A&A 489, 885–909 (2008)
DOI: 10.1051/0004-6361:200810044

Astronomy & Astrophysics

# A new stellar library in the region of the CO index at 2.3 $\mu$m

## New index definition and empirical fitting functions

E. Mármol-Queraltó[1], N. Cardiel[1], A. J. Cenarro[2], A. Vazdekis[2], J. Gorgas[1], S. Pedraz[3],
R. F. Peletier[4], and P. Sánchez-Blázquez[5]

[1] Departamento de Astrofísica y CC. de la Atmósfera, Universidad Complutense de Madrid, 28040 Madrid, Spain
e-mail: `emq@astrax.fis.ucm.es`
[2] Instituto de Astrofísica de Canarias, vía Láctea s/n, 38200 La Laguna, Tenerife, Spain
[3] Centro Astronómico Hispano Alemán, Calar Alto (CSIC-MPG), C/Jesús Durbán Remón 2-2, 04004 Almería, Spain
[4] Kapteyn Astronomical Institute, University of Groningen, Postbus 800, 9700 Av Groningen, The Netherlands
[5] Centre for Astrophysics, University of Central Lancashire, Preston PR1 2HE, UK

Received 24 April 2008 / Accepted 30 May 2008

### ABSTRACT

*Context.* The analysis of unresolved stellar populations demands evolutionary synthesis models with realistic physical ingredients and extended wavelength coverage.

*Aims.* We quantitatively describe the first CO bandhead at 2.3 $\mu$m to allow stellar population models to provide improved predictions in this wavelength range.

*Methods.* We observed a new stellar library with a better coverage of the stellar atmospheric parameter space than in earlier works. We performed a detailed analysis of the robustness of previous CO index definitions with spectral resolution, wavelength calibration, signal-to-noise ratio, and flux calibration.

*Results.* We define a new line-strength index for the first CO bandhead at 2.3 $\mu$m, $D_{\rm CO}$, better suited for stellar population studies than previous index definitions. We derive empirical fitting functions for the CO feature as a function of the stellar parameters ($T_{\rm eff}$, $\log g$ and [Fe/H]), showing a detailed quantitative metallicity dependence.

**Key words.** atlases – stars: fundamental parameters – globular clusters: general – galaxies: stellar content

## 1. Introduction

One of the most important challenges in modern astrophysics is the proper understanding of the stellar content of unresolved systems, such as extragalactic globular clusters and galaxies in different environments. Since the pioneering work of Crampin & Hoyle (1961) and Tinsley (1972, 1978, 1980), this has been accomplished through the comparison of the photometric and spectroscopic data with so-called evolutionary stellar population synthesis models, which make use of theoretical isochrones and libraries of spectral energy distributions (SEDs), either theoretical, empirical, or mixed (for more recent models, see e.g., Vazdekis et al. 2003; Bruzual & Charlot 2003; Maraston 2005). The most powerful approach to achieving this goal is to compare a number of observed line-strength indices with their model predictions, thereby providing constraints on the relevant physical properties of the systems: age, metallicity, initial mass function (IMF), and the relative abundance of different chemical species. Since the reliability of model predictions obviously improves as more realistic physical ingredients are included, an important effort has been devoted to improving the quality of the SED libraries. Theoretical libraries usually exhibit systematic discrepancies among themselves and in comparison with observational data (e.g., Lejeune et al. 1997, 1998). Although the alternative empirical libraries constitute a coarse-grained and usually incomplete (especially for non solar metallicities and non solar abundance ratios) sampling of the space of stellar atmospheric parameters, the use of empirical fitting functions (e.g., Gorgas et al. 1993, 1999; Worthey et al. 1994; Cenarro et al. 2002) can help to reduce these effects (e.g., Worthey 1994; Vazdekis et al. 2003).

To date, most of the observational effort has been focused on obtaining complete libraries in the optical range. However, a full understanding of the physical properties of integrated stellar systems cannot be achieved by ignoring other spectral windows. In this sense, the CO features in the $K$ band have been used by many researchers to investigate the stellar content of galaxies, including ellipticals (Frogel et al. 1975, 1978, 1980; Mobasher & James 1996, 2000; James & Mobasher 1999; Mannucci et al. 2001; Silva et al. 2008; Davidge et al. 2008), spirals (James & Seigar 1999; Bendo & Joseph 2004), compact galaxies (Davidge & Jensen 2007; Mieske & Kroupa 2008), starbursts and active galactic nuclei (Doyon et al. 1994; Ridgway et al. 1994; Shier et al. 1996; Puxley et al. 1997; Goldader et al. 1997; Vanzi & Rieke 1997; Mayya 1997; Ivanov et al. 2000; Hill et al. 1999; Riffel et al. 2007), among others. These strong absorptions are the bandheads formed in the first overtone ($\Delta\nu = +2$) bands of CO (Kleinmann & Hall 1986).

Despite the common use of these spectral features for stellar population studies, a proper characterization of the CO bands with stellar atmospheric parameters is still lacking. For that reason, we present in this work an improved study of the infrared region around 2.3 $\mu$m, where the first bandhead of the strong CO absorptions appears. In particular, we observed a new library of stars that clearly surpasses earlier works (see Sect. 2.1) in the coverage of the stellar atmospheric parameters. After a

Article published by EDP Sciences

**Table 1.** Main characteristics of previous spectroscopic stellar libraries in the $K$ band and the new stellar library presented in this work.

| Reference | Number of stars | Spectral range ($\mu$m) | Spectral resolution ($R = \lambda/\Delta\lambda$) | Spectral types | Notes |
|---|---|---|---|---|---|
| Johnson & Mendez (1970) | 32 | 1.2–2.5 | 550 | A–M, I–V | Low resolution |
| Kleinmann & Hall (1986) | 26 | 2.0–2.5 | 2500–3100 | F–M, I–V | Solar abundances |
| Lançon & Rocca-Volmerange (1992) | 56 | 1.4–2.5 | 550 | O–M, I–V | Low resolution |
| Ali et al. (1995) | 33 | 2.0–2.4 | 1380 | F–M, V | Dwarf stars |
| Hanson et al. (1996) | 180 | 2.0–2.2 | 800–3000 | O–B, I–V | Hot stars, not CO region |
| Wallace & Hinkle (1996) | 12 | 2.02–2.41 | ≥45 000 | G–M, I–V | Few stars |
| Ramirez et al. (1997) | 43 | 2.19–2.34 | 1380, 4830 | K–M, III | Giant stars |
| Wallace & Hinkle (1997) | 115 | 2.0–2.4 | 3000 | O–M, I–V | Solar abundances |
| Förster Schreiber (2000) | 31 | 1.90–2.45 | 830, 2000 | G–M I–III | Giant and supergiant stars |
| Lançon & Wood (2000) | 77 | 0.5–2.5 | 1100 | K–M, I–III | Giant and supergiant stars |
| Ivanov et al. (2004) | 218 | 1.48–2.45 | 2000–3000 | G–M, I–V | Not flux-calibrated |
| Hanson et al. (2005) | 37 | 2.0–2.2 | 8000–12000 | O–B, I–V | Hot stars, not CO region |
| Cushing et al. (2005) | 26 | 0.6–4.1 | 2000 | M–T, V | Extremely cold dwarf stars |
| Ranada et al. (2007) | 114 | 2.05–2.19 | 2200 | O–M, I–V | Not CO region |
| **This work** | 220 | 2.11–2.37 | 2500 | O–M, I–V | Improved metallicity coverage |

thorough analysis of previous index definitions that have been used to measure the first CO bandhead, we present a new index, $D_{\rm CO}$, which is well-suited to stellar population studies. This new index depends very little on spectral resolution (or velocity dispersion), is less sensitive to uncertainties in radial velocities, and can be measured with poorer signal-to-noise ratio (S/N).

In Sect. 2 we present the new stellar library, highlighting the improvements over previous libraries, the sample selection, an overview of the observations, and the data reduction. A detailed discussion of the $D_{\rm CO}$ index definition is given in Sect. 3. This section also includes a comparative study of the robustness of the new index to relevant effects. The measurements of the $D_{\rm CO}$ index for the stellar library and their associated error estimates appear in Sect. 4. Section 5 describes the stellar atmospheric parameters used to compute the fitting functions, which are derived in Sect. 6. Finally, Appendix A includes the tables with all the $D_{\rm CO}$ measurements for all the stars used for the fitting functions, as well as their stellar atmospheric parameters.

## 2. The new stellar library

### 2.1. Previous work

Several authors have compiled, for different purposes, spectroscopic stellar libraries in the $K$ band (Johnson & Mendez 1970; Kleinmann & Hall 1986; Lançon & Rocca-Volmerange 1992; Ali et al. 1995; Hanson et al. 1996; Wallace & Hinkle 1996, 1997; Ramirez et al. 1997; Förster Schreiber 2000; Lançon & Wood 2000; Ivanov et al. 2004; Hanson et al. 2005; Ranada et al. 2007). Table 1 summarizes the previous stellar libraries in the $K$ band, including the number of stars, spectral range, spectral resolution, and spectral types of the stars in each library. Due to the high S/N of their spectra, it is interesting to highlight the library of Kleinmann & Hall (1986) (hereafter KH86), which contains 26 stars, but only with solar abundances. Ivanov et al. (2004) present a library with 218 stars, which are not flux-calibrated. The poor metallicity coverage for these previous libraries (see Figs. 1 and 2) has not made it possible explore the metallicity dependence of the spectral features in the $K$ band.

### 2.2. Sample selection

We observed a new stellar library in the $K$ band that comprises 220 stars. The observed sample is a subset of MILES (Medium-resolution Isaac Newton Telescope Library of Empirical Spectra; Sánchez-Blázquez et al. 2006; Cenarro et al. 2007), a stellar library in the optical range with well known atmospheric parameters for all the stars (Cenarro et al. 2007). Our final stellar sample includes stars in the following stellar parameter ranges:

$$2485\ {\rm K} \leq T_{\rm eff} \leq 13404\ {\rm K},$$

$$-0.34\ {\rm dex} \leq \log g \leq 5.30\ {\rm dex},$$

$$-2.63\ {\rm dex} \leq [{\rm Fe/H}] \leq +0.98\ {\rm dex},$$

where $[{\rm Fe/H}] = \log Z - \log Z_{\odot}$.

This library clearly has a wider metallicity coverage than the previous ones (see Table 1 and Fig. 2 for a comparison between different works) and contains 8 stars in common with KH86, 23 with Wallace & Hinkle (1997) and 39 with Ivanov et al. (2004).

### 2.3. Observations and data reduction

The bulk of the stellar library (217 stars) was observed during a total of 13 nights in five observing runs from 2002 to 2005 on the 3.5 m telescope at Calar Alto Observatory (CAHA, Almería, Spain) with Ω-CASS. A subsample of the stellar library (52 stars) was observed again at the Telescopio Nazionale Galileo (TNG) at Roque de los Muchachos Observatory (La Palma, Spain) with NICS (Near Infrared Camera Spectrometer) in February 2006 and May 2007, plus 3 new stars. The details of the instrumental configuration for both runs are given in Table 2.

Each star was observed several times at different positions of the slit (standard procedure for infrared observations) to perform a reliable sky subtraction. Halogen lamps (on and off) and arc lamps were observed for flat-fielding, and C-distortion correction and wavelength calibration, respectively. Vega type (A0) stars were observed at different airmasses during each night in order to calibrate in relative flux and eliminate telluric lines in the stellar spectra.

We carried out a standard data reduction in the infrared using $\rm RED^{uc}_{m}E$ (Cardiel 1999), a reduction package that allows a parallel treatment of data and error frames. The reduction process includes flat-fielding, sky subtraction by subtracting consecutive images (A–B), cosmetic cleaning, C-distortion correction and wavelength calibration with arc lamps, spectrum extraction, and relative flux calibration. Atmospheric extinction was corrected by using extinction coefficients (namely the relative contributions of the Rayleigh scattering and the aerosol extinction)

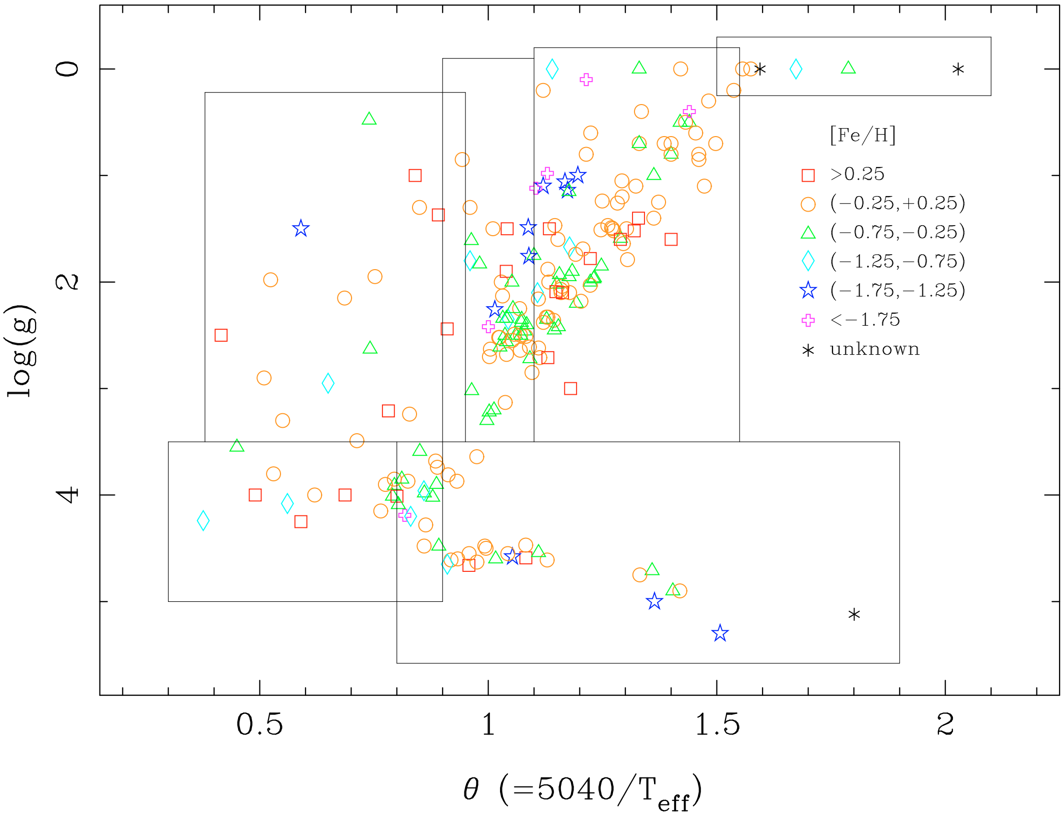

**Fig. 1.** $\log g - \theta$ diagram for the stellar library presented in this work, where $\theta = 5040/T_{\mathrm{eff}}$. Different symbols are used to indicate stars of different metallicities, as shown in the key. The boxes display the regions of the corresponding local fitting functions for the new CO index (see Sect. 6.2.2, for details).

derived for CAHA Observatory by Hopp & Fernández (2002). Those coefficients were extrapolated for La Palma Observatory to correct the stars observed in this observatory.

Some of the reduction steps that requires more careful work are explained in detail in the following sections.

### 2.3.1. Wavelength calibration

Arc spectra of Argon lamps were acquired to perform the C-distortion correction and the wavelength calibration. Due to instabilities and flexures of the instrument and the telescope, calibration arc frames were obtained after each star observed at CAHA. In the $K$ band, the typical number of known lines in the arc spectrum is rather low (just six in our instrumental configuration). Because of that, the wavelength calibration was not accurate enough and a second-order wavelength correction was performed by identifying OH air-glow lines in the sky spectrum of each star (Oliva & Origlia 1992; Rousselot et al. 2000). For observations at CAHA, a polynomial fit of the differences between the observed and theoretical OH lines for the sky spectrum was necessary. The wavelength calibration polynomial is expressed as a function of position as

$$W(x) = \lambda(x) + z(\lambda(x)), \tag{1}$$

where $\lambda(x)$ is the initial approximation to the wavelength calibration

$$\lambda(x) = \sum_{i=0}^{n} a_i x^i, \tag{2}$$

$x$ is the position in the spectral direction, and $a_i$ are the coefficients of the $n$th-degree calibration polynomial. The second-order correction is given by

$$z(\lambda(x)) = \sum_{j=0}^{m} b_j \lambda^j, \tag{3}$$

where $z(\lambda)$ are the computed differences between the observed and theoretical OH lines, and $b_j$ are the coefficients of a $m$th-degree polynomial. In our case, it is a second-order polynomial. The final wavelength calibration polynomial correction is

$$z(x) = \sum_{j=0}^{m} b_j \left( \sum_{i=1}^{n} a_i x^i \right)^j = \sum_{k=0}^{l} c_k x^k, \tag{4}$$

where $c_k$ are the coefficients of the new correction polynomial of order $l = m \cdot n$ as a function of the position $x$.

In the case of the observations at the TNG, we compared the observed sky spectrum with the well-calibrated sky spectrum from CAHA, and we observed constant wavelength differences between them. We cross-correlated both spectra and applied this constant shift to the wavelength calibration of TNG spectra.

Finally, we checked the final spectra with $K$ band spectra from KH86 and Wallace & Hinkle (1997), since they used a Fourier transform spectrometer, which implies a very accurate wavelength calibration of the spectra. Although in observations at CAHA no differences were obtained, for the TNG observations we had to apply a constant shift to achieve the correct wavelength calibration. The origin of this discrepancy is found in the lack of OH sky lines in the reddest wavelength region of the $K$ band, which prevented an accurate cross-correlation of the sky spectra in that region.

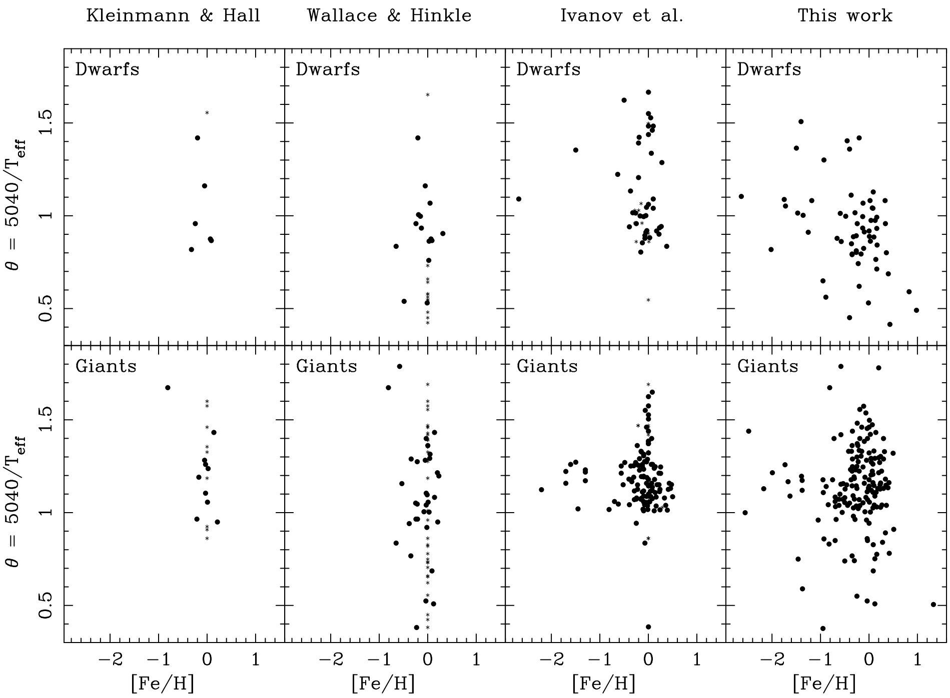

**Fig. 2.** Stellar parameter coverage in the stellar libraries of KH86, Wallace & Hinkle (1997), Ivanov et al. (2004), and this new library. We present separately dwarf and giant (and supergiant) stars (*upper and lower panels*, respectively). The stellar parameters of the stars from KH86 and Wallace & Hinkle (1997) were taken for Cayrel de Strobel et al. (2001) if available. Otherwise, we assigned solar metallicity and $T_{\rm eff}$ from their spectral type following the tables of Lang (1991) (small asterisks).

**Table 2.** Observational configurations.

| Telescope | CAHA 3.50 m | TNG 3.56 m |
|---|---|---|
| Instrument | Ω-CASS | NICS |
| Slit width (″) | 0.60 | 0.75 |
| Grism | #1 | KB |
| Filter | *K* | – |
| Spectral coverage | 2.01–2.43 $\mu$m | 1.95–2.34 $\mu$m |
| Dispersion | 2.527 Å/pix | 4.375 Å/pix |
| *FHWM* | 6.8 Å | 11.3 Å |
| Detector | Hawaii-I | Hawaii-I |

### 2.3.2. Flux calibration and telluric correction

There are two ways of flux-calibrating infrared spectra. The first method consists of observing a solar type star close to the star to be calibrated. The solar type star is reduced as usual, dividing the final spectrum by the solar spectrum (Livingston & Wallace 1991) degraded to the same spectral resolution as the problem star. In this way, a spectrum with the information about the response curve and the telluric lines is obtained. This spectrum is then rectified by the ratio between the blackbody spectra at the temperature corresponding to the solar type star and the solar temperature in order to obtain the correct continuum. This final spectrum is used to (relative) flux calibrate and carry out the telluric correction in the stars to be calibrated. The advantage of this method is that it is easy to find a star of this type for each observation.

A second method consists in the observation of Vega type stars at different airmasses during the night. The main reason for choosing these stars is that they are known to have no relevant features in our observational window, except the Br$\gamma$ line. After wavelength calibration, Vega type stars are divided by the well known theoretical Vega spectrum in our spectral range. In that way, a spectrum with both the response curve and the telluric corrections is obtained. The final stellar spectrum is then obtained after dividing each star by this spectrum. In this work, we have used this second approach.

### 2.3.3. Second-order telluric correction

As mentioned in the previous section, we used the flux standard star in order to not only flux-calibrate the stellar spectra, but also to correct simultaneously for the telluric absorption lines. Due to the variability of the observing conditions during the night, some telluric lines are badly corrected by applying the response curve derived from the flux standard star. For that reason an extra correction was necessary. First of all, we computed a reference spectrum with the information of the telluric lines. For observations at CAHA, we checked the response curves for each night looking for the spectrum with the best removal of telluric features. The ratio between each response curve and the previous spectrum free from telluric contamination provides the telluric spectra that we used to correct all the stellar spectra. In the case of the TNG observations, the telluric spectrum was obtained by dividing the flux standard spectra at high and low airmasses, observed during each night. The telluric spectrum in both observatories, obtained as explained above, consists mainly of differences in the strength of the telluric absorption lines. To correct for these lines, we modified their intensity by multiplying by an adjustable factor $K$, i.e.,

$$S_K = (S_0 - 1) \times K + 1, \qquad (5)$$

where $S_0$ is the telluric spectrum, and $S_K$ the telluric spectrum adjusted to correct a specific stellar spectrum. We divided the latter stellar spectrum by $S_K$ and computed the rms in the corrected spectrum. The best correction factor, $K$, is the one which minimizes the rms. This method was applied to different identified

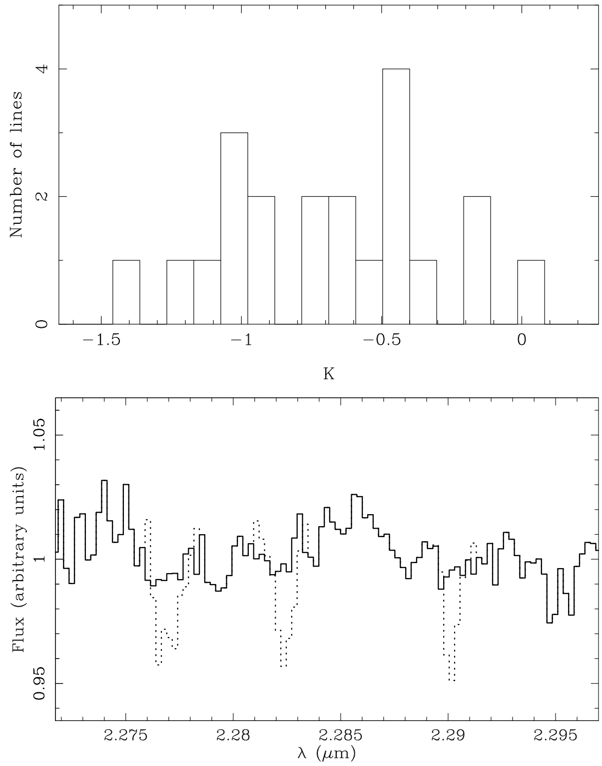

**Fig. 3.** *Upper panel*: histogram with the different $K$ factors (see Eq. (5)) employed to correct a particular stellar spectrum from telluric absorptions. *Lower panel*: example of a flux standard spectrum before (dotted line) and after (solid line) telluric correction (see details in the text).

telluric lines separately, since they do not vary in the same way. This effect can be seen in the histogram of Fig. 3, top panel, where the number of telluric lines corrected by a factor $K$ for a given spectrum is represented. In Fig. 3, bottom panel, we present an example of the telluric lines correction for a given flux standard spectrum. Notice that the telluric absorption lines can be present even after flux calibration and it is important to correct them in infrared spectroscopy.

## 3. Index definitions for the CO band at 2.3 $\mu$m

### 3.1. The K band region

The most prominent features in the $K$ band are caused by the rotational-vibrational transitions of the CO molecule around 2.3 $\mu$m. Important absorptions are also produced by other metallic species, such as Na I, Fe I, Ca I and Mg I (KH86, see Table 3). The only hydrogen line in this spectral range, Br $\gamma$, is present generally in absorption in O and B stars, going into emission for high-luminosity stars (for a detailed study of this kind of stars, see Hanson et al. 1996).

In this paper, we focus our study on the first CO bandhead at 2.29 $\mu$m. In contrast to the Ca I and Na I, the contribution of other species to the CO absorption is almost negligible (see Wallace & Hinkle 1996; Ramirez et al. 1997, for a further discussion).

### 3.2. Previous definitions

To measure the CO absorption at 2.3 $\mu$m in an objective way, several authors have proposed different index definitions. Baldwin et al. (1973) suggested a photometric system to measure the CO features based on two narrow filters ($\Delta\lambda$ = 0.10 $\mu$m) centered at 2.30 $\mu$m and at 2.20 $\mu$m for the CO absorption and the continuum, respectively. The CO index was defined as the difference of the two filters relative to the values obtained for $\alpha$ Lyrae, in magnitudes. Following this idea, Frogel et al. (1978) defined the most used photometric CO index (CO$_{\rm phot}$), with slightly different filter parameters ($\Delta\lambda$ = 0.08 $\mu$m, for the CO filter centered at 2.36 $\mu$m, and $\Delta\lambda$ = 0.11 $\mu$m for the filter centered at 2.20 $\mu$m for the continuum estimate).

**Table 3.** Main spectroscopic features in the $K$ band (from Kleinmann & Hall 1986).

| Species | $\lambda$ ($\mu$m) | Transition | Lower state energy (eV) |
|---|---|---|---|
| H I Br $\gamma$ | 2.1661 | $4^2F^0{-}7^2G$ | 12.70 |
| Na I | 2.2062 | $4s^2S_{1/2}{-}4p^2P^0_{1/2}$ | 3.19 |
| Na I | 2.2090 | $4s^2S_{1/2}{-}4p^2P^0_{3/2}$ | 3.19 |
| Fe I | 2.2263 | $x^5F^0_4{-}e^5D_3$ | 5.07 |
| Fe I | 2.2387 | $x^5F^0_3{-}e^5D_2$ | 5.04 |
| Ca I | 2.2614 | $4d^3D_{3,2,1}{-}4f^3F^0_4$ | 4.68 |
| Ca I | 2.2631 | $4d^3D_{3,2,1}{-}4f^3F^0_3$ | 4.68 |
| Ca I | 2.2657 | $4d^3D_{3,2,1}{-}4f^3F^0_2$ | 4.68 |
| Mg I | 2.2814 | $4d^3D_{3,2,1}{-}6f^3F^0_{2,3,4}$ | 6.72 |
| $^{12}$CO(2, 0) | 2.2935 | (2, 0) bandhead | 0.62 |
| $^{12}$CO(3, 1) | 2.3226 | (3, 1) bandhead | 0.86 |
| $^{13}$CO(2, 0) | 2.3448 | (2, 0) bandhead | 0.32 |
| $^{12}$CO(4, 2) | 2.3524 | (4, 2) bandhead | 1.12 |

The first spectroscopic CO index ($\mathrm{CO}^{\rm mag}_{\rm KH}$) for the CO(2, 0) bandhead at 2.3 $\mu$m was defined by KH86 as

$$\mathrm{CO}^{\rm mag}_{\rm KH} = -2.5 \log\ \mathrm{CO}_{\rm KH} = -2.5 \log\ \frac{\mathcal{F}_{\rm a}}{\mathcal{F}_{\rm c}}, \tag{6}$$

where $\mathrm{CO}_{\rm KH} = \mathcal{F}_{\rm a}/\mathcal{F}_{\rm c}$ is the ratio between the fluxes integrated over narrow wavelength ranges centered in the absorption line ($\lambda\lambda$2.29305−2.29832 $\mu$m) and the nearby continuum ($\lambda\lambda$2.28728−2.29252 $\mu$m), measured in magnitudes. These band limits have been used to measure the index as an equivalent width (e.g. Origlia et al. 1993). Both measurements can be converted using (Origlia & Oliva 2000)

$$\mathrm{CO}^{\rm mag}_{\rm KH} = -2.5 \log \left(1 - \frac{W_\lambda (2.29)}{53\ \text{Å}}\right), \tag{7}$$

where $\mathrm{CO}^{\rm mag}_{\rm KH}$ is the spectroscopic index initially defined by KH86 measured in magnitudes, and $W_\lambda$ (2.29) is the same index measured as an equivalent width.

Doyon et al. (1994) studied the behavior of CO$_{\rm phot}$ and indicated several reasons to introduce their new spectroscopic definition

$$\mathrm{CO}_{\rm sp} = -2.5\ \log\langle R_{2.36}\rangle, \tag{8}$$

where $\langle R_{2.36}\rangle$ is the mean value of the rectified spectrum (normalized in the continuum) in the 2.31−2.40 $\mu$m range. This rectified spectrum is obtained by fitting the continuum in the 2.00−2.29 $\mu$m range with a power law ($F_\lambda \propto \lambda^{-\alpha}$), due to the similarity of the stellar spectrum in the $K$ band to a Rayleigh-Jeans law. As Origlia & Oliva (2000) indicated, this index is just the equivalent width over the CO range relative to a continuum that is extrapolated from shorter wavelengths. As a main advantage, this definition allows measurements of the CO even from poor quality spectra.

Other authors (for example, Lançon & Rocca-Volmerange 1992; Ramirez et al. 1997; Förster Schreiber 2000) proposed their own definitions, adopting the bandpasses for the absorption and the continuum without considering the use of those definitions in general situations. Recently, Riffel et al. (2007) measured the CO absorption at 2.3 $\mu$m as an equivalent width between $\lambda\lambda 2.2860{-}2.3100\,\mu$m, computing a continuum defined as a spline using points free of emission/absorption lines in the broad interval $\lambda\lambda 2.2350{-}2.3690\,\mu$m.

After a study of different band limits for the CO index measured in terms of equivalent widths for stars of different spectral types, Puxley et al. (1997) proposed to extend the absorption band of KH86 up to the end of the CO (2, 0) band (2.320 $\mu$m), and the use of three different bands to estimate the continuum ($\lambda\lambda 2.253{-}2.261$ $\mu$m, 2.270–2.278 $\mu$m, and 2.285–2.291 $\mu$m). This type of index definition is what Cenarro et al. (2001a) called a *generic index*. Puxley et al. (1997) adopted this definition because it allows giant and supergiant stars to be distinguished, and the correction for velocity dispersion is less than with the other definitions.

An additional definition was introduced by Frogel et al. (2001), in which the CO absorption feature is measured using multiple bandpasses to estimate the pseudo-continuum level.

### 3.3. New index definition

Even though the number of different CO index definitions is large, we have explored in detail whether any of these is actually well-suited to practical study of this spectroscopic feature in the integrated spectra of galaxies. Curiously, from the list of previous index definitions, only the one presented by Puxley et al. (1997) (based on the previous definition by KH86) was designed to take the variations in the index with radial velocity and velocity dispersion into account, both of them very important in the study of galaxies. In this work we made an additional effort to investigate the possibility of finding an optimal CO index definition that could improve all the previous definitions.

To carry out this task, we focused our efforts on defining a CO index that is less sensitive to low S/N, degradation due to spectral resolution and/or velocity dispersion, errors in wavelength calibration (or errors in radial velocity), and in relative flux calibration (see the next sections for a further study of each case).

After exploring different possibilities for the definition of the new index, we propose to measure the CO at 2.29 $\mu$m as a *generic discontinuity*, i.e., as the ratio between the average fluxes in the continuum and in the absorption bands

$$\mathrm{D}_{\mathrm{generic}} \equiv \frac{\dfrac{\sum_{i=1}^{n_{\mathrm{c}}} \int_{\lambda_{\mathrm{c},i_1}}^{\lambda_{\mathrm{c},i_2}} F_{\mathrm{c},i}(\lambda)\;\mathrm{d}\lambda}{\sum_{i=1}^{n_{\mathrm{c}}} (\lambda_{\mathrm{c},i_2} - \lambda_{\mathrm{c},i_1})}}{\dfrac{\sum_{i=1}^{n_{\mathrm{a}}} \int_{\lambda_{\mathrm{a},i_1}}^{\lambda_{\mathrm{a},i_2}} F_{\mathrm{a},i}(\lambda)\;\mathrm{d}\lambda}{\sum_{i=1}^{n_{\mathrm{a}}} (\lambda_{\mathrm{a},i_2} - \lambda_{\mathrm{a},i_1})}} \tag{9}$$

where $D_{\mathrm{generic}}$ is the generic discontinuity, and $F_{\mathrm{a},i}(\lambda)$ and $F_{\mathrm{c},i}(\lambda)$ are the flux in the $n_{\mathrm{a}}$ absorption bands and $n_{\mathrm{c}}$ continuum bands, respectively. Finally, $\lambda_{x,i_1}$ and $\lambda_{x,i_2}$ are the lower and upper wavelength limits of the $i$th band $x$ (where $x$ is a or c). This new definition is similar to the B4000 index defined by Gorgas et al. (1999) but using more than one bandpass to define the continuum and the absorption regions.

**Table 4.** Spectroscopic CO index definitions.

| Index | Continuum bands ($\mu$m) | Absorption bands ($\mu$m) | Comments |
|---|---|---|---|
| $\mathrm{CO}^{\mathrm{mag}}_{\mathrm{KH}}$ | 2.2873–2.2925 | 2.2931–2.2983 | Color-like index |
| $I_{\mathrm{Puxley}}$ | 2.2530–2.2610<br>2.2700–2.2780<br>2.2850–2.2910 | 2.2931–2.3200 | Generic index |
| $I_{\mathrm{Frogel}}$ | 2.2300–2.2370<br>2.2420–2.2580<br>2.2680–2.2790<br>2.2840–2.2910 | 2.2910–2.3020 | Generic index |
| $D_{\mathrm{CO}}$ | 2.2460–2.2550<br>2.2710–2.2770 | 2.2880–2.3010 | Generic discontinuity |

References are $\mathrm{CO}^{\mathrm{mag}}_{\mathrm{KH}}$ (Kleinmann & Hall 1986), $I_{\mathrm{Puxley}}$ (Puxley et al. 1997) and $I_{\mathrm{Frogel}}$ (Frogel et al. 2001). Wavelengths are in vacuum.

Here we propose to measure the CO feature at 2.3 $\mu$m as a generic discontinuity, $D_{\mathrm{CO}}$, using two bandpasses for the continuum ($n_{\mathrm{c}} = 2$) and one bandpass for the absorption region ($n_{\mathrm{a}} = 1$). The limits of these bands are also listed in Table 4. We selected the number of bandpasses and their location taking into account several factors. Concerning the continuum bandpasses, we have eluded the Ca I and Mg I features, trying not to extend too far towards shorter wavelengths to avoid potential systematic effects arising in the flux calibration of wide line-strength indices. In the case of the absorption region, one single bandpass is enough to cover the first CO bandhead. Compared with previous definitions, we decided to shift the blue continuum bandpass limit slightly to obtain an index that is more stable with velocity dispersion (i.e. spectral resolution) and with radial velocity uncertainties.

Following Cardiel et al. (1998), it is not difficult to show that the expected variance in a $D_{\mathrm{generic}}$ index can be computed as

$$\sigma^2[D_{\mathrm{generic}}] = \frac{\mathcal{F}_{\mathrm{c}}^2 \sigma^2_{\mathcal{F}_{\mathrm{a}}} + \mathcal{F}_{\mathrm{a}}^2 \sigma^2_{\mathcal{F}_{\mathrm{c}}}}{\mathcal{F}_{\mathrm{a}}^4}, \tag{10}$$

where $\mathcal{F}_x$ is the total flux per wavelength unit in the continuum ($x$ = c) and the absorption ($x$ = a) region, determined from the coaddition of the flux in all the corresponding bandpasses, i.e.,

$$\mathcal{F}_x \equiv \Theta \frac{\sum_{i=1}^{n_x} \sum_{k=1}^{N^i_{\mathrm{pixels}}} F_{x,i}(\lambda_k)}{\sum_{i=1}^{n_x} (\lambda_{x,i_2} - \lambda_{x,i_1})}, \tag{11}$$

with $n_x$ the number of bandpasses in either the continuum or the absorption region, $\Theta$ is the linear dispersion (in Å/pixel), $N^i_{\mathrm{pixels}}$ is the number of pixels covered by the $i$th bandpass of the $x$ region (with $x$ equal to c or a), and $\lambda_k$ is the central wavelength of the $k$th pixel. The variance in these total fluxes are simply

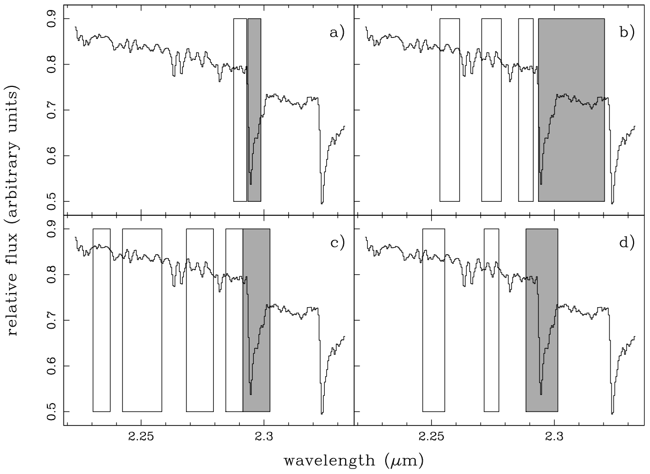

**Fig. 4.** Limits of the bandpasses in the definitions for the CO index proposed by: **a)** KH86, **b)** Puxley et al. (1997), **c)** Frogel et al. (2001), and **d)** the new CO index presented in this work. Grey and open bands represent absorption and continuum bandpasses, respectively, for each index definition, superimposed on the spectrum of HD 137704.

computed as the quadratic sum of the individual variances in each pixel, i.e.,

$$\sigma^2_{\mathcal{F}_x} = \Theta^2 \frac{\sum\limits_{i=1}^{n_x} \sum\limits_{k=1}^{N^i_{\rm pixels}} \sigma^2_{F_{x,i}}(\lambda_k)}{\left[\sum\limits_{i=1}^{n_x} (\lambda_{x,i_2} - \lambda_{x,i_1})\right]^2}, \qquad (12)$$

where, in particular, $\sigma^2_{F_{x,i}}(\lambda_k)$ is the variance corresponding to the random error in the $k$th pixel. It is important to highlight that in these expressions we are assuming that the random errors in each pixel are not correlated.

### 3.4. Sensitivities of the indices to different effects

In this section, we discuss the sensitivity of previous spectroscopic indices defined by KH86 ($\mathrm{CO}^{\rm mag}_{\rm KH}$), Puxley et al. (1997) ($I_{\rm Puxley}$), and Frogel et al. (2001) ($I_{\rm Frogel}$), and the new CO index ($D_{\rm CO}$) to velocity dispersion (or spectral resolution), wavelength calibration (radial velocity), relative flux calibration, and S/N. A fifth index, $D_{\rm Frogel}$, is considered: a generic discontinuity based on the same bands proposed by Frogel et al. (2001). In Fig. 4 we show the bandpasses for these index definitions. For this study, we selected from the high-resolution library of Wallace & Hinkle (1996) three stars with similar spectral type (M 2–5; chosen because of their strong CO features) and different luminosity class (supergiant, giant and dwarf) to account for differences depending on the type of star. The resolution of the spectra is 0.54 Å (*FHWM*) and they are all shifted to rest-frame.

#### 3.4.1. Spectral resolution and velocity dispersion broadening

To study the sensitivity of the spectroscopic CO indices to the spectral resolution or velocity dispersion broadening ($\sigma$), we broadened the stellar spectra of the selected stars with additional $\sigma$'s from the initial $\sigma_0$ up to $\sigma = 400$ km s$^{-1}$ (in steps of 10 km s$^{-1}$). The different indices were measured on all these broadened spectra and we computed the ratio between the index ($I$) at each $\sigma$ and the index measured on the original spectrum ($I_0$). Figure 5 (left column) shows this ratio as a function of the velocity dispersion for the definitions we are studying. Compared to the other index definitions, the two generic discontinuities ($D_{\rm Frogel}$ and $D_{\rm CO}$) are clearly the least sensitive to velocity dispersion broadening.

#### 3.4.2. Wavelength calibration

Sometimes, errors in the wavelength calibration arise in the spectra even after a very careful reduction or due to an inaccurate radial velocity ($v_{\rm r}$) estimate of the studied object. Because of that, it is important to define indices with the least possible sensitivity to this kind of uncertainty. To quantify this effect, we measured the CO absorption with the different index definitions in the stellar spectra shifted from −200 to +200 km s$^{-1}$ with steps of 4 km s$^{-1}$ in radial velocity. In Fig. 5 (central column) we present the ratio between the index, $I$, measured at $v_{\rm r}$ and the initial value $I_0$ (assumed $v_{\rm r} = 0$ km s$^{-1}$) as a function of the considered $v_{\rm r}$ for different types of stars. It is apparent from the figures that the indices $\mathrm{CO}^{\rm mag}_{\rm KH}$, $I_{\rm Puxley}$ and $I_{\rm Frogel}$ are very sensitive to radial velocity uncertainties, while $D_{\rm Frogel}$ and the new index definition $D_{\rm CO}$ are more robust to this effect.

#### 3.4.3. Flux calibration

As explained in Sect. 2.3.2, it is common to use theoretical spectra to recover the real shape of the continuum. This practice implies the knowledge of the temperatures of the standard stars. For that reason, we studied the impact, during flux calibration, of an error in the temperature estimate of the standard stars. To analyze the impact when solar-type stars are used as flux standards, we computed the blackbody spectrum in the interval $5600 \leq T_{\rm eff} \leq 6300$ K, and derived the ratio between these spectra and the blackbody at solar temperature. To study the effect when Vega type stars are used as calibrators, we analyzed the differences from the theoretical spectrum of Vega ($T_{\rm eff} \sim 9400$ K) and the real temperature of the Vega type stars (from 8400 to 14 400 K for our study). In both cases, we found that the changes in the continuum produced by differences in the assumed temperature of standard stars produce negligible differences in the measured indices.

Finally, we studied the impact of a wrong curvature in the response curve, which is a typical source of systematic error. To obtain an estimate of this effect, as a first-order approach we artificially modified the continuum shape of the original spectra by multiplying them by a second-order polynomial. This polynomial was chosen to pass through 3 fixed points, two at the borders of the wavelength range (where the polynomial were forced to be equal to 1.0), and another point at the center of that range (where the polynomial was set to a variable parameter $\beta$ ranging from 0.5 to 1.5). In Fig. 6 we show different examples of these polynomials for distinct values of $\beta$. With this exercise, we simply studied the effect of a low frequency error in flux calibration.

In Fig. 5 (right column) we present the ratio between the measured index in the stellar spectrum multiplied by the polynomial for a given value of $\beta$, $I$, and the original one, i.e., $I_0$ for $\beta = 1.0$ (no additional curvature), as a function of the parameter $\beta$. The sensitivity of each index definition to the $\beta$ parameter is, not surprisingly, dependent on the location and wavelength coverage of the index bandpasses, and also depends on the way the pseudo-continuum is determined and on the absolute value of the index. For these reasons, $\mathrm{CO}^{\rm mag}_{\rm KH}$, $I_{\rm Puxley}$, and $I_{\rm Frogel}$ are the

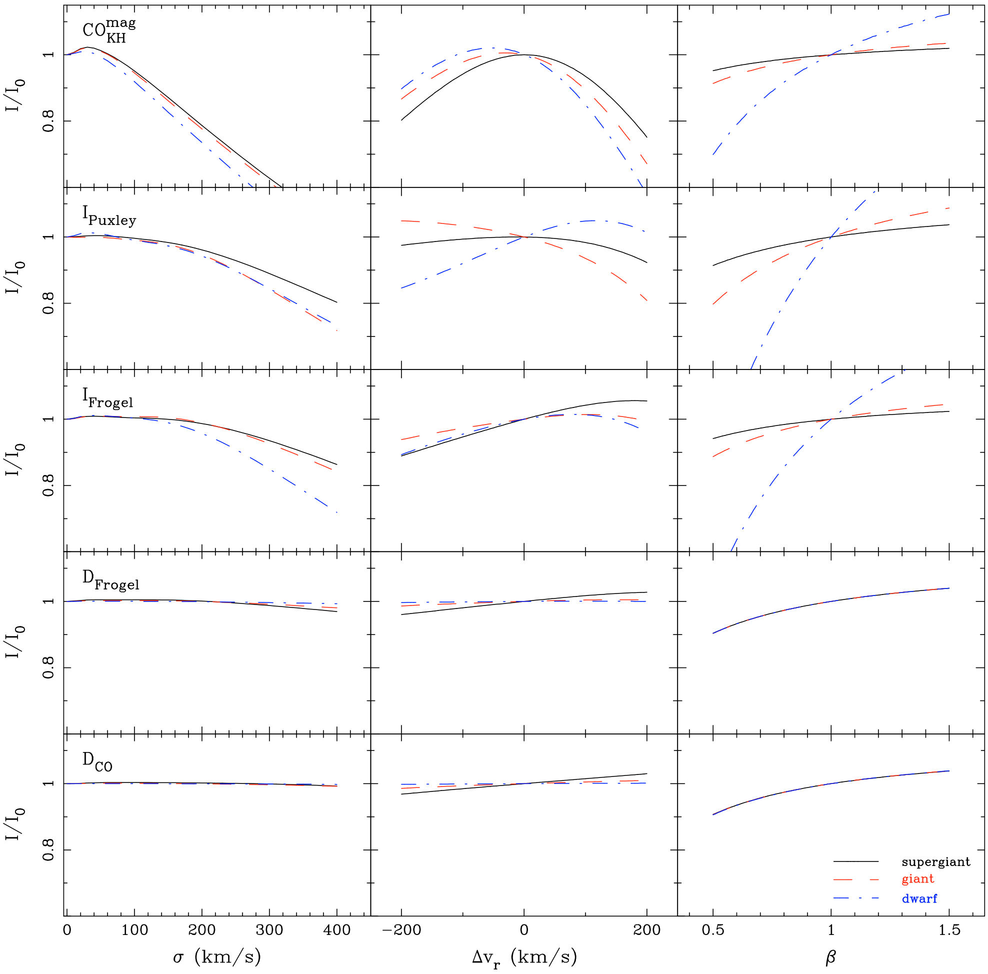

**Fig. 5.** Study of the sensitivity of the different CO index definitions (*from top to bottom*, $\mathrm{CO}^{\mathrm{mag}}_{\mathrm{KH}}$, $I_{\mathrm{Puxley}}$, $I_{\mathrm{Frogel}}$, $D_{\mathrm{Frogel}}$ and $D_{\mathrm{CO}}$) to several relevant parameters. *Left column*: ratio between the index $I$ measured on the spectra broadened with a given $\sigma$, and the index $I_0$ measured on the initial spectra ($\sigma_0 = 3$ km s$^{-1}$, corresponding to the resolution of the stellar library of Wallace & Hinkle 1996). *Central column*: ratio between the index $I$ for a given $v_{\mathrm{r}}$ and the index $I_0$ in the original spectrum ($v_{\mathrm{r}} = 0$ km s$^{-1}$). *Right column*: ratio between the index $I$ measured on the spectrum multiplied by a curved spectrum parametrized by $\beta$ (see Sect. 3.4.3 for details) and the index measured over the original spectrum, $I_0$, as a function of the curvature parameter $\beta$.

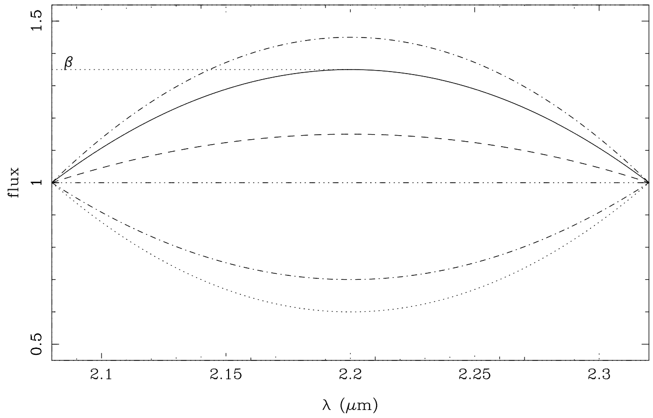

**Fig. 6.** Examples of the curved spectra used in the study of the sensitivity of the different index definition to a wrong curvature of the spectrum. The parameter $\beta$ determines the distance to the maximum/minimum in the center of the spectrum (shown here for the polynomial displayed with a solid line).

most sensitive to an error in the response curve. In particular, the $\mathrm{CO}^{\mathrm{mag}}_{\mathrm{KH}}$ depends strongly on the strength of the CO absorption. On the other hand, $I_{\mathrm{Puxley}}$ and $I_{\mathrm{Frogel}}$, defined as generic indices, extrapolate the continuum value into the absorption band and, in that way, the wrong curvature. In addition, the generic discontinuities $D_{\mathrm{Frogel}}$ and $D_{\mathrm{CO}}$, computed as the averaged flux in the continuum and absorption bands, exhibit no differences between dwarf, giant, and supergiant stars.

### 3.4.4. S/N ratio

One important issue in the definition of a new index is the dependence of the relative error of the measurements on the S/N. In this sense, the aim is to find an index definition that provides the lowest relative error in the measurements with the lowest S/N in the spectra. For that reason, we studied the behavior of relative errors measured with previously analyzed CO index definitions as a function of the S/N. Using a particular stellar spectrum, we simulated a set of one hundred spectra (and their associated error spectra) with random S/N(Å) ratios in the range 1.0−100.0. For this task we used the program `indexf`[1] (Cardiel 2007). In Fig. 7 we compare the results obtained for a giant star (same results

---

[1] `http://www.ucm.es/info/Astrof/software/indexf/`

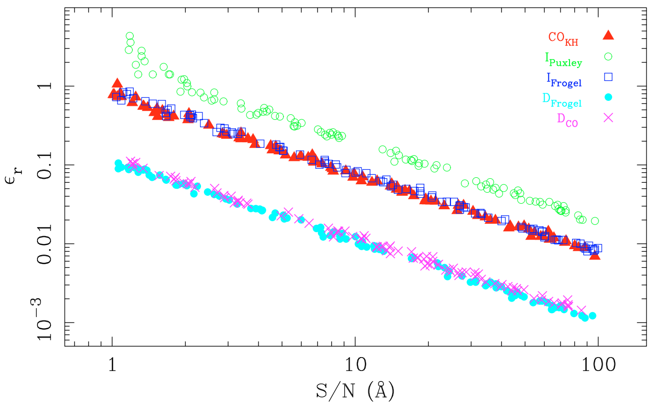

**Fig. 7.** Example of the study of the dependence of the relative error in the measure of the first CO bandhead using different index definitions at a given S/N per Å. We represent the relative errors vs. S/N (in logarithmic scale) measured on the simulated spectra of a giant star (the results are independent of the type of star). Different symbols are used to indicate different index definitions, as shown in the key. See text for details.

**Table 5.** Values of the constant $c$ of Eq. (13) for the different index definitions analyzed in Sect. 3.4.

| Index | $c$ |
|---|---|
| $\mathrm{CO}_{\mathrm{KH}}^{\mathrm{mag}}$ | 0.7537 |
| $I_{\mathrm{Puxley}}$ | 2.0258 |
| $I_{\mathrm{Frogel}}$ | 0.8123 |
| $D_{\mathrm{Frogel}}$ | 0.1075 |
| $D_{\mathrm{CO}}$ | 0.1198 |

are obtained for supergiant and dwarf stars). Not surprisingly, the relative errors in all the definitions follow

$$\varepsilon_{\mathrm{r}} = \frac{c}{S/N(\text{Å})}, \tag{13}$$

where $c$ is a constant that depends on the particular index. This result has already been found for atomic and molecular indices (Cardiel et al. 1998), and for generic indices (Cenarro et al. 2001a). It is clear from Fig. 7 that the same holds for generic discontinuities. Considering Eq. (13), it is evident that, at a given S/N, the lower relative errors correspond to the index definitions with lower $c$ values. Table 5 list these values for the five index definitions under study. From these numbers and the data displayed in Fig. 7, it is obvious that $D_{\mathrm{CO}}$ is comparable to $D_{\mathrm{Frogel}}$, while $\mathrm{CO}_{\mathrm{KH}}^{\mathrm{mag}}$, $I_{\mathrm{Puxley}}$ and $I_{\mathrm{Frogel}}$ provide larger relative errors for a given S/N.

### 3.4.5. The best index definition

Once we have studied the behavior of the different CO index definitions as a function of all the relevant parameters, we can conclude that the $D_{\mathrm{CO}}$ index definition is, in general, preferable. On one hand, $\mathrm{CO}_{\mathrm{KH}}^{\mathrm{mag}}$, $I_{\mathrm{Frogel}}$, and $I_{\mathrm{Puxley}}$ are too sensitive of spectral resolution and errors in wavelength calibration and radial velocity. In addition, the behavior of $\mathrm{CO}_{\mathrm{KH}}^{\mathrm{mag}}$, $I_{\mathrm{Frogel}}$ and $I_{\mathrm{Puxley}}$ are also too sensitive to uncertainties in the spectrophotometric system (i.e., flux calibration).

When the sensitivity to S/N is included in the comparison, it is clear that the best definitions are the two generic discontinuities, namely $D_{\mathrm{Frogel}}$ and $D_{\mathrm{CO}}$. Since the use of generic discontinuities for measuring the CO absorption is introduced for the first time in this paper, and considering that the $D_{\mathrm{CO}}$ is practically insensitive to spectral resolution (or velocity dispersion broadening) up to $\sigma \sim 400$ km s$^{-1}$, we propose to use the new definition, especially for the future analysis of integrated spectra.

### 3.5. Conversion between different CO index systems

In this section we give the calibrations to convert between the new CO index definition and the CO indices defined by KH86, Puxley et al. (1997) and Frogel et al. (2001). In order to obtain these conversions, we measured the indices on the subsample of stars observed at the TNG ($3200 \leq T_{\mathrm{eff}} \leq 9625$ K, $0.00 \leq \log g \leq 5.00$, $-1.73 \leq [\mathrm{Fe/H}] \leq +0.36$). The calibrations were computed by deriving a least squares fit to the data. The fits are completely compatible with index measurements on the KH86 and Wallace & Hinkle (1997) spectra which are on the same spectrophotometric system. Just six stars from Wallace & Hinkle (1997) deviate more than $3\sigma$ from the fitted relation due to a problems in the continuum and the telluric correction of those spectra. In Fig. 8 we show all these fits and the data used to compute them.

The conversion between the index defined by KH86, $\mathrm{CO}_{\mathrm{KH}}^{\mathrm{mag}}$, and the new index $D_{\mathrm{CO}}$ is given by

$$D_{\mathrm{CO}} = 1.0407\,(\pm 0.0021) + 0.2317\,(\pm 0.0035)\ \mathrm{CO}_{\mathrm{KH}}^{\mathrm{mag}} \tag{14}$$

with $r^2 = 0.9863$.

The expression to compute $D_{\mathrm{CO}}$ from the index defined by Frogel et al. (2001) is

$$\begin{aligned} D_{\mathrm{CO}} &= 1.0507\,(\pm 0.0031) + 0.0077\,(\pm 0.0005)\ I_{\mathrm{Frogel}} \\ &\quad +0.00007\,(\pm 0.00002)\ I_{\mathrm{Frogel}}^2 \end{aligned} \tag{15}$$

with $r^2 = 0.9802$, where $I_{\mathrm{Frogel}}$ is measured as an equivalent width (Å).

As we mentioned before, $I_{\mathrm{Puxley}}$ is also measured as an equivalent width. The expression to compute the $D_{\mathrm{CO}}$ index from $I_{\mathrm{Puxley}}$ is

$$D_{\mathrm{CO}} = 1.0488\,(\pm 0.0033) + 0.0051\,(\pm 0.0001)\ I_{\mathrm{Puxley}} \tag{16}$$

with $r^2 = 0.9629$.

Finally, we also computed the conversion between the ratio $\mathrm{CO}_{\mathrm{KH}}$ (not to be confused with $\mathrm{CO}_{\mathrm{KH}}^{\mathrm{mag}}$; see Eq. (6)) and the new CO index

$$\begin{aligned} D_{\mathrm{CO}} &= 2.1119\,(\pm 0.0724) - 1.6205\,(\pm 0.1772)\ \mathrm{CO}_{\mathrm{KH}} \\ &\quad +0.5521\,(\pm 0.1071)\ \mathrm{CO}_{\mathrm{KH}}^2 \end{aligned} \tag{17}$$

with $r^2 = 0.9867$. This last transformation will be used in next section.

## 4. Measurements of the CO absorption for the stellar library and error estimates

### 4.1. Index measurements

A detailed study of the continuum in spectra observed at CAHA compared with the the spectra published by KH86 revealed some problems with the flux calibration of the CAHA data. The shape of the continuum in these spectra showed a spurious and non-reproducible high-frequency structure superimposed to the real continuum, which was affecting not only the shape of the continuum but also the final index measurements. During the reduction

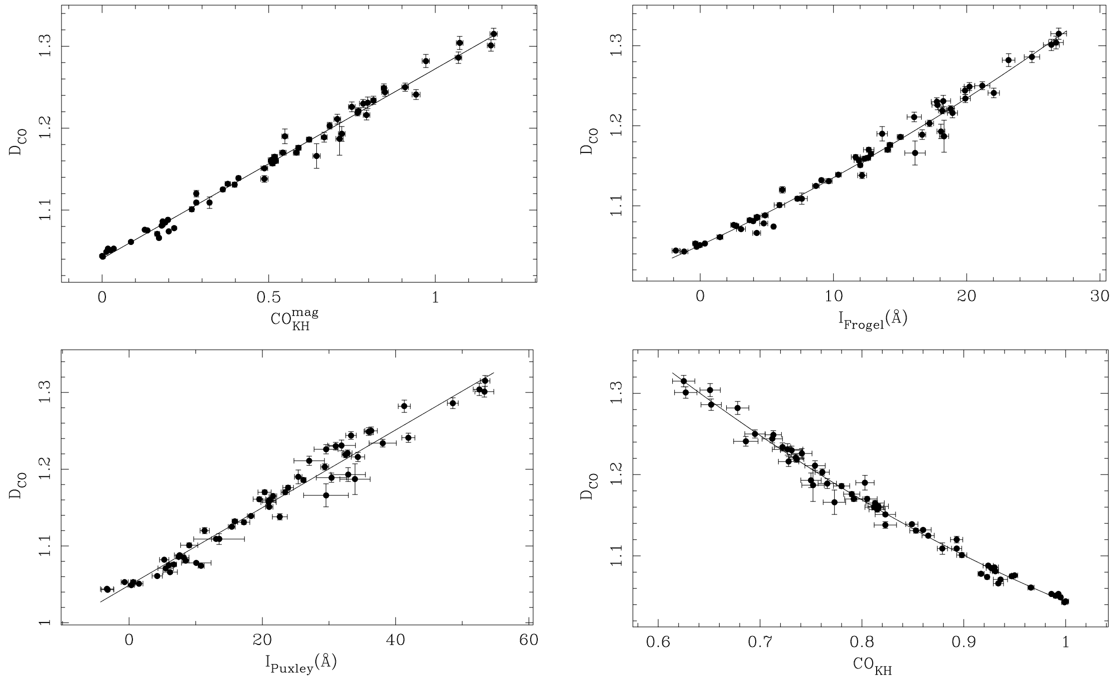

**Fig. 8.** Comparison between measurements on the TNG subsample of the first CO bandhead using different index definitions. The panels show the transformation between the new index $D_{\rm CO}$ and $\mathrm{CO}_{\rm KH}^{\rm mag}$, $I_{\rm Frogel}$, $I_{\rm Puxley}$ and $\mathrm{CO}_{\rm KH}$ (*from top to bottom*, and *from left to right*). The solid lines are least squares fits to the data, and correspond to the transformations given in Eqs. (14)–(17).

of the data it was neither possible to identify nor correct this additional source of noise.

In order to handle, at least in an empirical way, the spectrophotometric calibration of the CAHA spectra, we re-observed a good subsample of the stellar library at the TNG. To guarantee that the TNG data were on the appropriate spectrophotometric system, the CO measurement of each star observed at the TNG was compared with the measurement of the most similar spectrum (in $T_{\rm eff}$ and luminosity class) available in the KH86 library at the same spectral resolution.

Since the bandpasses for the new index $D_{\rm CO}$ encompass a wide range in wavelength, the strange behavior of the continuum shape in the CAHA spectra has a large impact on the index measurements. Luckily, this is not such a big issue for the $\mathrm{CO}_{\rm KH}$ ratio, since both continuum and absorption bandpasses are very close in this definition. For that reason, we decided to measure the $\mathrm{CO}_{\rm KH}$ index, transforming afterward the results into the $D_{\rm CO}$ index using Eq. (17) (which provides a good conversion between both indices, as shown in the previous section). In more detail, the method to derive the final spectrophotometric calibration can be summarized as follows.

First of all, the $\mathrm{CO}_{\rm KH}$ measurements of the subsample of stars with solar metallicity re-observed at the TNG were compared with the corresponding star in the KH86 library, as explained before. In Fig. 9, left panel, the results of this comparison are shown. A least squares fit to the one-to-one relation was computed, providing $r^2 = 0.9768$. Although some points in this figure appear relatively far from the 1:1 relation (considering their error bars), it is important to highlight that we are not comparing the same stars, and that, in any case, the determination coefficient $r^2$ is high enough to guarantee the quality of the transformation.

Finally, we used the stars in common between the TNG and CAHA to empirically correct the measured indices on the CAHA spectra sampled at the spectral resolution of the TNG spectra. Figure 9, right panel, presents the relation between the $\mathrm{CO}_{\rm KH}$ ratio in common stars observed in both observatories. A least squares fit to a straight line gives $r^2 = 0.9539$. We checked that a unique empirical correction is valid for all the observing runs at CAHA (within the statistical errors). For this study, we used all the individual measurements for each star instead of averaging all the observations along the slit. After transforming the CAHA $\mathrm{CO}_{\rm KH}$ measurements onto the correct spectrophotometric system, we applied Eq. (17) to obtain the new $D_{\rm CO}$ measurements, which will be used later to derive the empirical fitting functions.

## 4.2. Random errors and systematic effects

### 4.2.1. Known sources of random errors

We considered several sources of random errors: photon statistic and read-out noise, errors due to the detector cosmetic, the combined effect of wavelength calibration and radial velocity uncertainties, and flux calibration uncertainties.

(*i*) *Photon statistics and read-out noise*. With the aim of tracing the propagation of photon statistic and read-out noise, we followed a parallel reduction of data and error frames with the reduction package $\mathrm{RED}^{\mathrm{uc}}_{\mathrm{m}}\mathrm{E}$, which creates error frames at the beginning of the reduction procedure and translates into them, by following the law of combination of errors, all the manipulations performed over the data frames. In this way the most problematic reduction steps (flat-fielding and distortion corrections, wavelength calibration, etc.) are taken into account and, finally, each data spectrum has its corresponding error spectrum which can be used to derive reliable photon errors in the index ($\sigma_{\rm photon}$). A detailed description of the estimate of random errors in the measurement of classical line-strength indices and the impact of their interpretation are shown in Cardiel et al. (1998, 2003). The new CO index is defined in this paper as

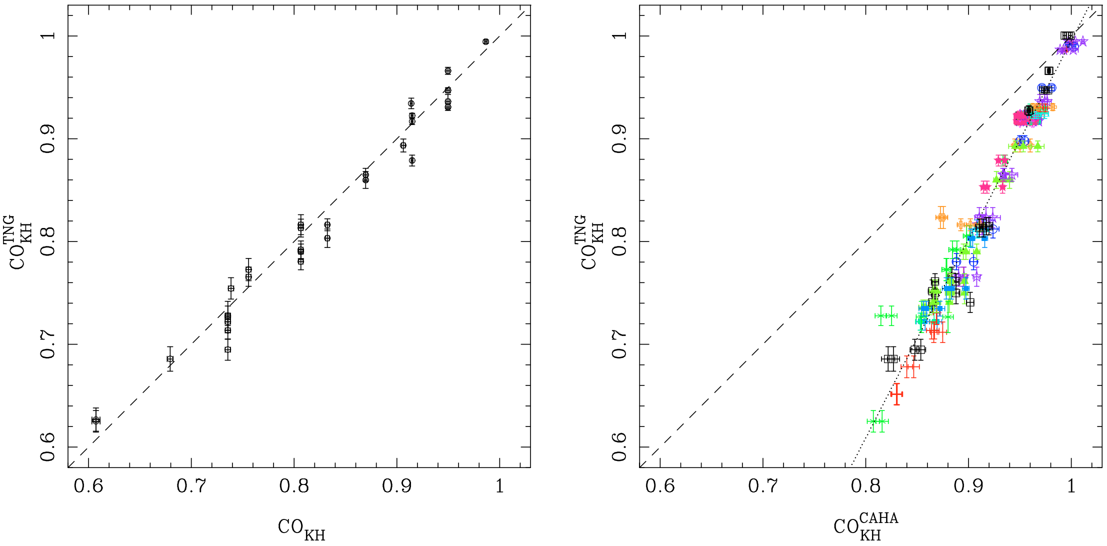

**Fig. 9.** *Left panel*: $CO_{KH}$ index measured on the stars with solar metallicity observed at the TNG ($CO_{KH}^{TNG}$) vs. the same measurements in the most similar stars from the KH86 library ($CO_{KH}$). *Right panel*: $CO_{KH}$ index measured on stars observed in common at TNG ($CO_{KH}^{TNG}$) and CAHA ($CO_{KH}^{CAHA}$). Different symbols are used for distinct observing runs at CAHA, although no segregation of the data between runs is apparent. The dotted line shows the empirical correction for the CAHA measurements. In both panels, the dashed line shows the one-to-one relation.

a *generic discontinuity* and follows the expressions given in Sect. 3.3 for the errors.

($ii$) *Errors due to the detector cosmetic*. In the case of infrared detectors, the errors due to the detector cosmetic are very important. We measured the rms (*root-mean-squared*) on two different regions of the spectra with no apparent absorption features ($\lambda\lambda$2.2685–2.2790 $\mu$m and $\lambda\lambda$2.2825–2.2890 $\mu$m), in order to obtain an estimation of photon statistics and read-out noise errors together with the errors due to imperfections present in the images even after flat-fielding correction. In Fig. 10 we compare the errors due to photon statistic and read-out noise errors (upper panel), derived from first principles (using the parallel reduction of data and error frames), with the errors from direct measurement of the rms in the spectra (lower panel). As it can be seen, we are underestimating the random errors if we do not consider the errors due to the detector cosmetic.

($iii$) *Wavelength calibration and radial velocity errors*. The combined effect of wavelength calibration and radial velocity correction is another random source of error. We considered as an upper limit for the wavelength calibration error the projection on the spectral direction of half of the slit width. These values were measured from the *FWHM* of the arc lines, providing errors of 45 km s$^{-1}$ for the observations at CAHA and 85 km s$^{-1}$ for the TNG images. These numbers translate into typical errors of $\sigma[D_{\rm CO}]$ = 0.002 and $\sigma[D_{\rm CO}]$ = 0.004, for CAHA and TNG respectively.

Radial velocity for most of the stars in the stellar library were taken from the Hipparcos Input Catalogue (Turon et al. 1992), which in the worst cases are given with mean probable errors of 5 km s$^{-1}$. For the missing stars in this catalogue, we adopted radial velocities from the SIMBAD database, which presents typical errors of a few km/s. These errors are completely negligible in comparison with the wavelength calibration errors already mentioned.

($iv$) *Flux calibration errors*. In order to check for possible random errors in the index measurements due to the flux calibration method, we should have observed several spectrophotometric reference spectra each observing night. Since this is a highly time-consuming approach, we did not observe them. Alternatively, we decided to check the impact of this kind of error through the comparison of common stars between different nights and runs and we will discuss it in Sect. 4.2.3.

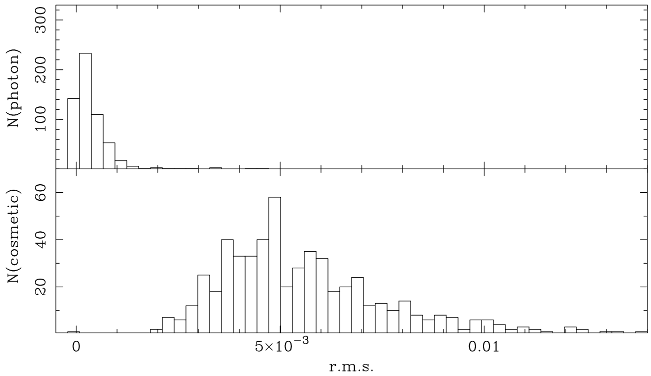

**Fig. 10.** *Upper panel*: histogram with the photon statistic and read-out noise error in the $D_{\rm CO}$ for the stars in the stellar library. *Lower panel*: similar histogram with the errors derived from measurements of the rms on two spectral regions with no apparent absorption features for the stars in the stellar library.

### 4.2.2. Additional sources of random errors

Expected random errors for each star can be computed by adding quadratically the random errors derived from the known sources previously discussed, i.e.,

$$\sigma^2[{\rm CO}]_{\rm initial} = \sigma^2[{\rm CO}]_{\rm photon+cosmetic} + \sigma^2[{\rm CO}]_{\rm wavelength}. \quad (18)$$

However, additional (but unknown) sources of random errors may still be present in the data. Using the multiple observations available for each particular star, we compared the standard deviation of the different $D_{\rm CO}$ measurements ($\sigma[{\rm CO}]_{\rm rms}$) with the initial random error ($\sigma^2[D_{\rm CO}]_{\rm initial}$) for that star. In the cases in which the standard deviation was significantly larger than the expected error (using a $\chi^2$-test of variances), a residual random error $\sigma[D_{\rm CO}]_{\rm residual}$ was derived as

$$\sigma^2[{\rm CO}]_{\rm residual} = \sigma^2[{\rm CO}]_{\rm rms} - \sigma^2[{\rm CO}]_{\rm initial}, \tag{19}$$

and quadratically added to the initial random errors to obtain the final random errors, i.e.,

$$\sigma^2[{\rm CO}]_{\rm final} = \sigma^2[{\rm CO}]_{\rm initial} + \sigma^2[{\rm CO}]_{\rm residual}. \tag{20}$$

It is worth noting that this additional error was only necessary for a few stars, since most of them presented consistent errors between different measurements.

#### 4.2.3. Systematic effects

Due to the large number of runs needed to complete the whole library, systematic errors can arise because of possible differences between the spectrophotometric systems of each run at both the CAHA and TNG telescopes. To guarantee that the whole dataset is on the same system, we observed stars in common between different runs at each telescope. We compared the index measurements of these stars by applying a *t*-test to study whether the differences of the index measurements of the common stars were statistically larger than zero, finding no systematic effects between different nights within a given observing run, and between different runs. For that reason we considered that an additional error exclusively due to flux calibration was not required (i.e., the actual flux calibration errors are within the already computed random errors).

It is important to highlight that there is not guarantee that our data are on a *true* spectrophotometric system, so we encourage readers interested in using our results to include in their observing plan stars in common with the stellar library to ensure a proper comparison.

### 4.3. Additional measurements of the CO absorption: globular cluster stars

To improve the stellar parameter coverage of our stellar library, additional stars were included for the computation of empirical fitting functions for the $D_{\rm CO}$ (see Sect. 6). Frogel et al. (2001) and Stephens & Frogel (2004) presented a sample of globular cluster giant stars ($R \sim 1500$, $\sigma \sim 85$ km s$^{-1}$), characterized by their low metallicity, with measurements of the CO absorption at 2.3 $\mu$m using the definition of Frogel et al. (2001). Since there is not dependence of $I_{\rm Frogel}$ at the spectral resolution of these data (see Fig. 5), we transformed their CO measurements to the new index by applying Eq. (15). The stellar atmospheric parameters of these stars were determined from $J$ and $K$ photometry, as it is explained in Sect. 5.2. Finally, we considered 80 stars from Frogel et al. (2001) and 14 stars from Stephens & Frogel (2004), which, together with the stellar library presented in this work, will be used to parametrize the behavior of the CO index as a function of the stellar atmospheric parameters.

## 5. Stellar atmospheric parameters

In this section, we present the atmospheric parameters for the stars considered in the computation of the empirical fitting functions for the $D_{\rm CO}$ index presented in Sect. 6.

### 5.1. Atmospheric parameters for the observed stellar library sample

As we mentioned before, the stellar library presented in this work is a subsample of the MILES library (Sánchez-Blázquez et al. 2006). Following the previous work by Cenarro et al. (2001b), a reliable and highly homogeneous data set of atmospheric stellar parameters for the stars in MILES library was derived by Cenarro et al. (2007) as the result of a previous, extensive compilation from the literature and a carefully calibration and correction by bootstrapping of the data on to a reference system. In short, the method can be itemized in the following steps (see Cenarro et al. 2001b; and Cenarro et al. 2007, for a more detailed explanation of the working procedure): (i) selection of a high-quality, standard reference of atmospheric parameters; (ii) bibliographic compilation of atmospheric parameters of the stars in the library; (iii) calibration and correction of systematic differences between the different sources and the standard reference system; and (iv) determination of averaged, final atmospheric parameters for the library stars from all those references corrected on to the reference system. Together with the atmospheric parameters, an estimation of the uncertainties in their determination is given for each star. In that way, stellar atmospheric parameters (and their uncertainties) are perfectly well known for the stars in the new stellar library.

### 5.2. Atmospheric parameters for the additional globular cluster stars

For the subsample of 94 red giant branch (RGB) stars from Galactic globular clusters, effective temperatures ($T_{\rm eff}$) and surface gravities ($\log g$) were derived from $J$ and $K$ photometry, following a technique similar to that explained in Cenarro et al. (2007, see also Cenarro et al. 2001b). Absolute, reddening corrected photometry for all clusters was taken from Frogel et al. (2001) and Stephens & Frogel (2004).

The surface gravity for each cluster star was estimated by matching its location in a $M_K - (J - K)$ diagram to the appropriate isochrones from Girardi et al. (2000) (see Fig. 11), whose colors and magnitudes were previously transformed to the observational plane using the empirical color-temperature relations for giant stars from Alonso et al. (1999) and Lejeune et al. (1997, 1998), with the latter being for giants with $T_{\rm eff} \leq 3500$ K (see more details in Vazdekis et al. 2003).

If available, the metallicity for each cluster was taken from the work by Rutledge et al. (1997, hereafter RHS97), which provides metallicity estimates for Galactic globular cluster on the Carretta & Gratton (1997, hereafter CG97) scale based on the Ca II triplet strengths of their RGB stars. This was the case for NGC 0104, NGC 0288, NGC 0362, NGC 5927, NGC 6553, NGC 6624, NGC 6712, and M6 9. For M 71, however, we kept the value in the CG97 scale inferred by Cenarro et al. (2002) according to the CaT indices of their stars. If not available in RHS97, metallicity values in the (Zinn & West 1984, hereafter ZW84) scale were transformed into the CG97 scale using Eq. (7) in CG97. This was the case for the rest of our GC sample. For NGC 6388, NGC 6440, Liller1, and Terzan2, ZW84 metallicity values were taken from Table 6 in that paper. For NGC 6528, the value given in the 2003 revised version of the catalog of parameters for Milky Way globular clusters (Harris 1996) was employed. It is important to note that there is a double reason for using the CG97 metallicity scale in this work. First, since, as compared to the Zinn & West (1984) metallicity scale, the agreement between the locus of the cluster RGB stars and the

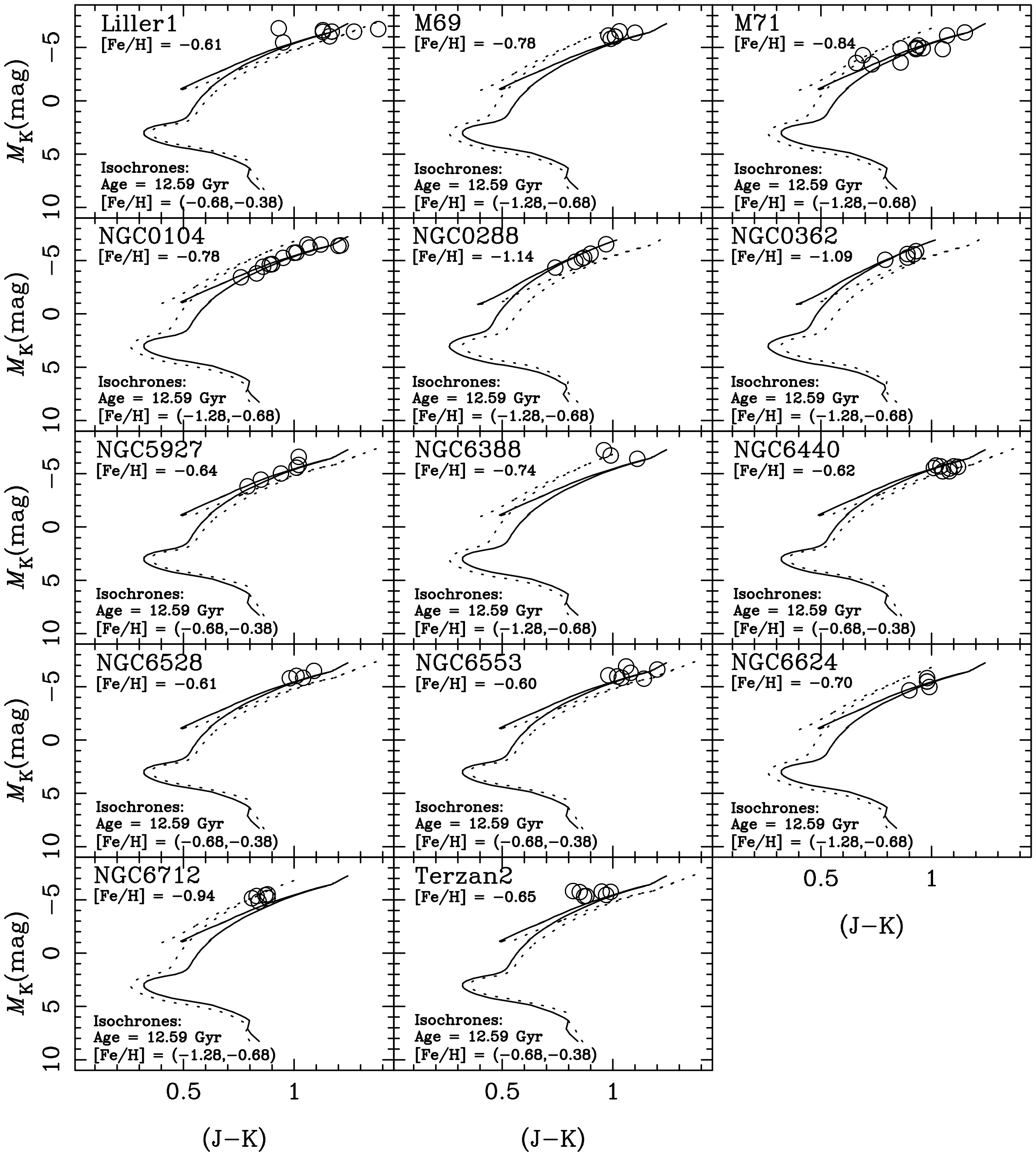

**Fig. 11.** Pseudo-HR diagrams for the cluster stars together with adequate isochrones (Girardi et al. 2000; Lejeune et al. 1997, 1998) for each individual cluster. Open circles are used for individual stars in the clusters. Solid and dashed lines illustrate isochrones of 12.59 Gyr and two metallicity values enclosing the one of the cluster (as shown in the labels). Adopted metallicities for the clusters are labeled in the figure. In all cases, the solid line is employed to indicate the isochrone whose metallicity is closer to that of the cluster. Surface gravity for each star was estimated by comparing to the predicted $M_K$ as explained in Sect. 5.2. Final atmospheric parameters for each cluster star, and their corresponding errors, are given in Table A.2.

corresponding isochrones in the $M_K-(J-K)$ plane is much better when using CG97 values, particularly in the high metallicity regime. Also, because the metallicities of the rest of cluster stars in this paper (as taken from either Cenarro et al. 2001b, 2007) are already on the CG97 scale, thus guaranteeing full consistency among the metallicities of the whole star sample, and minimizing systematics in the computation of the fitting functions.

Assuming that all the galactic globular cluster under study are similarly old, and taking into account the above metallicities, for all the stars in each cluster we used two of the Girardi's isochrones of 12.6 Gyr with metallicities enclosing the corresponding value of the cluster (solid and dashed lines in Fig. 11). For each isochrone, a $\log g$ value for each star was estimated by interpolating in $M_K$. Final $\log g$ values were computed as weighted means of the single values derived from the two different metallicity isochrones, with weights accounting for the differences between the adopted cluster metallicity and the isochrone values.

Effective temperatures for all the cluster giants were computed on the basis of the $(J-K)-T_{\rm eff}$ relations given in Alonso et al. (1999) (for $T_{\rm eff} > 3500$ K) and Lejeune et al. (1997, 1998) (for $T_{\rm eff} \leq 3500$ K). Interestingly, since Alonso's relation for

$(J-K)$ does not depend on either metallicity and $\log g$, $T_{\rm eff}$ can be directly determined from $(J-K)$. This indeed helps to minimize the sources of uncertainties in the final temperatures of most globular cluster giants. As a matter of fact, only a few temperatures for very cold stars were computed using Lejeune's relations.

Errors for the derived atmospheric parameters of the cluster stars were estimated from input uncertainties in [Fe/H] and in the photometric data employed in this technique. For those [Fe/H] values taken from RHS97 and Cenarro et al. (2002), the uncertainties given therein were assumed. For the rest of the clusters, metallicity errors were computed from those given in ZW84 through standard error propagation in Eq. (7) of CG97. Since most stars in Frogel et al. (2001) and Stephens & Frogel (2004) were selected from the bright ends of the globular cluster luminosity functions, photometric observational errors in $J$ and $K$ bands turned out to be very small ($\ll$0.06 mag; see e.g. Frogel et al. 1995; Kuchinski et al. 1995; Kuchinski & Frogel 1995) as compared to typical uncertainties in the assumed distance moduli and reddening corrections. Errors in $M_K$, and $(J-K)$ are therefore strongly dominated by the above effects. For this reason, typical errors of 0.20 mag and 0.06 mag for $M_K$ and $(J-K)$, respectively, have been considered for all the cluster stars.

Final values of $T_{\rm eff}$, $\log g$, [Fe/H], and their corresponding errors for the whole sample of cluster stars are presented in Table A.2.

## 6. Empirical calibration of the new CO index

In this section we parametrize the behavior of the new CO index in terms of the stellar atmospheric parameters ($T_{\rm eff}$, $\log g$ and [Fe/H]. For that purpose, we use the $D_{\rm CO}$ index measurements of the stars of the new stellar library and on the sample of globular cluster stars from Frogel et al. (2001) and Stephens & Frogel (2004) (see Sect. 4.3). This paper shows a detailed quantitative metallicity dependence of the CO feature at 2.3 $\mu$m.

### 6.1. Behaviour of the CO index as a function of stellar atmospheric parameters

The dependence of the strong CO absorption bands as a function of the effective temperature and surface gravity is well known from the first studies in the infrared (KH86; Johnson & Mendez 1970; Frogel et al. 1978; Lançon & Rocca-Volmerange 1992; Doyon et al. 1994; Wallace & Hinkle 1997; Ramirez et al. 1997; Förster Schreiber 2000; Lançon & Wood 2000; Ivanov et al. 2004; Silva et al. 2008). The CO absorptions turn deeper as the stars are cooler, while hot stars show no trace of CO features. On the other hand, as surface gravity decreases, the CO absorptions become prominent, i.e., supergiant stars present more important CO absorption than dwarfs. All the previous works in the $K$ band highlighted both the tight correlation of their defined CO indices with temperature (spectral type or $J-K$ color in the first papers), and the dependence of the CO absorption with surface gravity. In addition, a few theoretical studies (McWilliam & Lambert 1984; Origlia et al. 1993) indicate that these spectroscopic features should be metallicity dependent. Terndrup et al. (1991) showed that Baade's window stars have deep 2.3 $\mu$m bands, what they interpreted as these stars probably having a high metallicity. Model predictions by Maraston (2005) also show the dependence of the CO absorptions in the $K$ band with metallicity. Observations of composite stellar population (e.g. Origlia & Oliva 2000; Riffel et al. 2007) give support to this dependence. Unfortunately, the lack of empirical stellar libraries with an appropriate coverage in metallicity had prevented, until now, a detailed quantitative description of this dependence. Figure 12 shows, graphically, how the first CO bandhead at 2.3 $\mu$m varies with the stellar atmospheric parameters ($T_{\rm eff}$, $\log g$ and [Fe/H]).

Several authors have partially parametrized the described behavior of the first CO bandhead. Lançon & Rocca-Volmerange (1992) computed a relation of their CO index with the color temperature of giant stars. Doyon et al. (1994) parametrized the behavior of their CO index with the effective temperature for supergiant, giant and dwarf stars, separately. More recently, Ramirez et al. (1997) used their CO index to obtain effective temperatures for giants. They applied the same method to dwarf stars from Ali et al. (1995). However, there is no systematic study of the dependence of the CO absorption as a function of the atmospheric stellar parameters due to the poor stellar parameter coverage of previous libraries, especially in metallicity. In the next subsection we compute an empirical calibration for the $D_{\rm CO}$ index measured for the stars of our stellar library which accounts for the previously described qualitative behavior of the CO absorption.

### 6.2. Fitting functions

To reproduce the behavior exhibited by a given feature, empirical calibrations of the corresponding line-strength index as a function of the stellar atmospheric parameters were derived. These calibrations, called fitting functions, are just a mathematical description of the observed behavior and there is not physical justification for the explanation of each of the significant terms in such fitting functions. We use $\theta = 5040/T_{\rm eff}$ as temperature indicator, together with $\log g$ and [Fe/H] as parameters for gravity and metallicity. Following previous works (Gorgas et al. 1993; Worthey et al. 1994; Gorgas et al. 1999; Cenarro et al. 2002), two possible functional forms for the computation of the fitting functions are typically considered, in particular

$$I\,(\theta, \log g, [{\rm Fe/H}]) = p\,(\theta, \log g, [{\rm Fe/H}]) \qquad (21)$$

and

$$I\,(\theta, \log g, [{\rm Fe/H}]) = {\rm const.} + \exp[p\,(\theta, \log g, [{\rm Fe/H}])\,, \qquad (22)$$

where $I$ refers to a given index, and $p\,(\theta, \log g, [{\rm Fe/H}])$ is a polynomial with terms up to the third order, including all possible cross-terms among the three parameters, i.e.

$$p\,(\theta, \log g, [{\rm Fe/H}]) = \sum_{0\leq i+j+k\leq 3} c_{i,j,k}\,\theta^i\ (\log g)^j\ [{\rm Fe/H}]^k\,, \qquad (23)$$

with $0 \leq i+j+k \leq 3$ and $0 \leq i, j, k$.

The optimum fitting function is the one which minimizes the residuals of the fits, i.e., when the differences between the measured index ($I_{\rm obs}$) and the index predicted by the fitting function ($I_{\rm pred}$) are the lowest.

In general, not all the terms in Eq. (23) are necessary for reproducing the dependences of an index on the stellar parameters. To obtain the significant terms for the best fitting functions, we follow two different approaches (Cenarro et al. 2002). Both of them consist of an iterative and systematic procedure based on the computation of a general fit together with the analysis of the residual variance of the fit and estimated errors of each fitted coefficient, for a given set of stars with well known atmospheric parameters, index measurement and error. The significance of each term considered in the fit is calculated by means of a $t$-test (that is, using the error in that coefficient to check whether it is

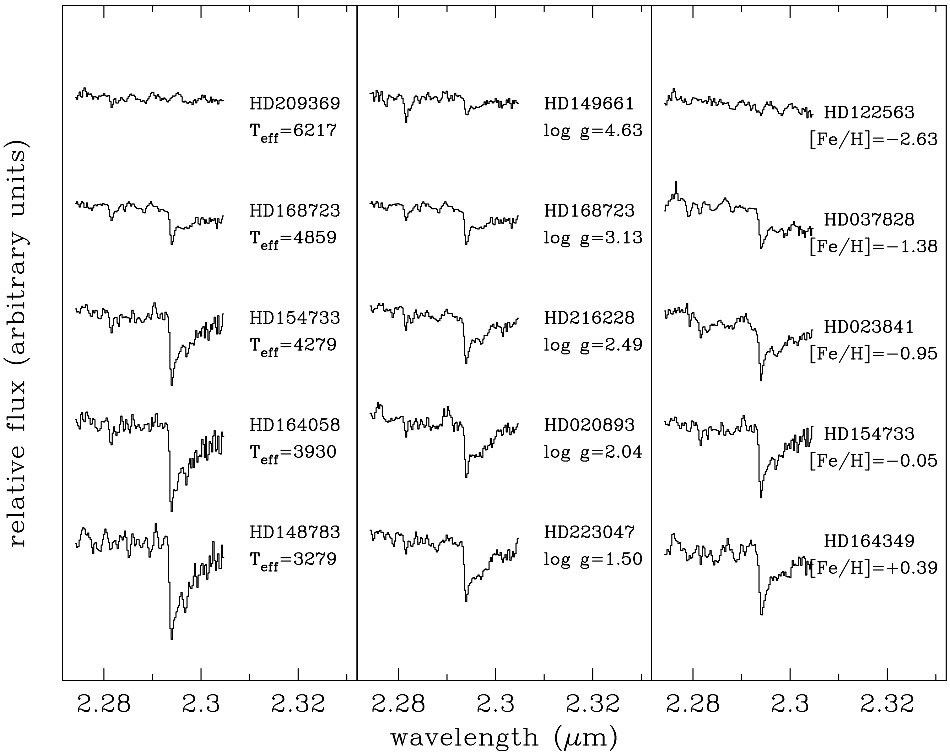

**Fig. 12.** Behaviour of the first CO bandhead with $T_{\text{eff}}$, $\log g$ and [Fe/H] (*from left to right*). In each case, the displayed stars have been selected to exhibit a range in a given atmospheric parameter (as shown in the labels) with similar values for the other two parameters.

significantly different from zero). Typically, we consider a term as significant for a threshold value of the significance level parameter $\alpha = 0.10$. The first method consists of computing the fit with all the terms in Eq. (23) and eliminating, during each iteration, the least significant term. A parallel method consists of computing an initial one-parameter fit and incorporating new terms only when they are significant. Together with this criterion, we study the residuals derived for each set of terms. The final fit will be the one that minimizes the sum of the residuals while having all the employed $c_{i,j,k}$ coefficients statistically significant, which does not produce systematic deviations in the residuals for stars of different types, e.g., stars of a given metallicity range, and that reproduces the observed behavior of the index.

### 6.2.1. The general fitting procedure

As a result of the wide stellar parameter coverage of the library, there is not a single fitting function able to reproduce the whole behavior of the $D_{\text{CO}}$ index. For that reason, we divided the stellar parameter space into several ranges (boxes) where local fitting functions have been computed following the methods explained in the previous section. The final fitting function for the whole parameter space is then constructed by considering the derived local fitting functions. In some ranges, an overlapping region in a generic parameter $z$ has been allowed between two different boxes. If $I_1(x, y, z)$ and $I_2(x, y, z)$ are two local fitting functions defined respectively in the intervals $(z_{1,1}, z_{1,2})$ and $(z_{2,1}, z_{2,2})$ with $z_{2,1} < z_{1,2}$, the final predicted index $I(x, y, z)$ in the overlapping region is obtained by interpolating the index value in both boxes, i.e.,

$$I(x, y, z) = wI_1(x, y, z) + (1 - w) I_2(x, y, z), \tag{24}$$

where the weight $w$ is modulated by the distance to the overlapping limits as

$$w = \frac{z - z_{2,1}}{z_{1,2} - z_{2,1}}, \tag{25}$$

or

$$w = \cos\left[\frac{\pi}{2}\left(\frac{z - z_{2,1}}{z_{1,2} - z_{2,1}}\right)\right], \tag{26}$$

for a cosine-weighted mean, where $z_{2,1} \leq z \leq z_{1,2}$.

### 6.2.2. Fitting functions for the $D_{\text{CO}}$ index

Figure 13 shows the behavior of the $D_{\text{CO}}$ index versus $\theta$ for the stars in the new library. There is a clear dichotomy in the behavior of stars depending on their gravity. For that reason, we divided the stellar atmospheric parameter space in two main groups: dwarf stars ($\log g > 3.5$ dex) and giant and supergiant stars ($\log g < 3.5$ dex). As we explained in Sect. 6.1, there is also a strong dependence of the CO absorption with the effective temperature. That is why we subdivided each gravity group into different temperature ranges. Independently of their gravity, stars with high effective temperature exhibit no traces of CO absorptions and their index value tends to a constant ($D_{\text{CO}} \simeq 1.05$). On the other hand, due to the lack of very cold stars in both gravity regimes, we computed a constant value of the index for cold dwarf and giant stars. In short, we considered three temperature ranges for dwarf stars, while we considered four different ranges for the giants (see Table 6). The boundaries of these ranges are shown in Fig. 1. In some cases, an overlapping region has been considered. After some experimentation in order to obtain the smoothest fit, we computed the final index in the intersection region considering a different weight $w$ depending on the case (see Table 6).

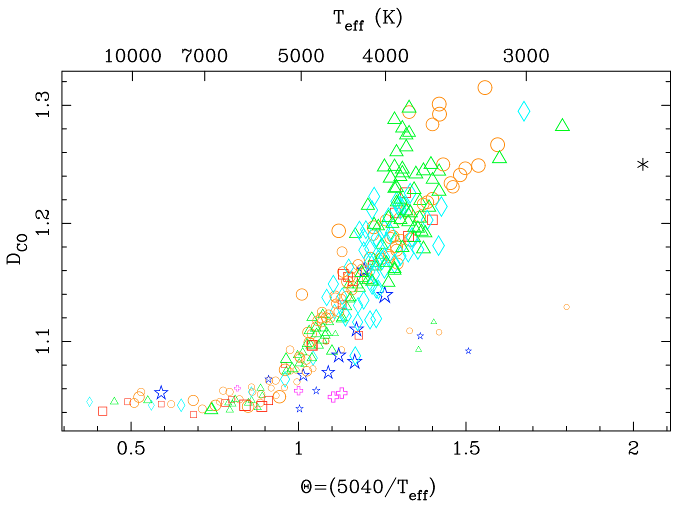

**Fig. 13.** $D_{\rm CO}$ index as a function of $\theta$ (=5040/$T_{\rm eff}$) for the stars of the new library plus the globular cluster stars from Frogel et al. (2001) and Stephens & Frogel (2004) used in this study. Symbols mean metallicity, as explained in Fig. 1. Relative symbol sizes indicate gravity ranges (small symbols for dwarfs, increasing symbol size for decreasing gravity).

Besides the global behavior described for giant stars, two different trends are found for this type of stars around $\theta$ = 1.3−1.4 in Fig. 13. After a carefully study of these stars with a higher CO index, we found that they are stars in the asymptotic giant branch (AGB). For that reason, we decided to compute an independent fit for these stars in the range $\theta$ = 1.01−1.56, shown in Fig. 14 (coefficient in Table 6). Since there are no AGB stars for $\theta > 1.56$, we simply extrapolate the constant value of the CO index at $\theta = 1.56$.

Up to now, we described the general method to compute fitting functions. However, we used a slightly different method for cold and warm giant stars. First of all, we obtained constant fits for hot ($\theta < 0.90$) and cold stars ($\theta > 1.55$) as explained before. After this, we generated a set of fake stars with random gravity and metallicity and effective temperature of $\theta = 5040/T_{\rm eff} = 1.60$. Their index values were evaluated from the fitting function computed for cold giant stars. For the associated error of the indices of these fake stars, we assumed the mean error of the cold stars. We calculated the local fitting function of cool giants, including these new stars. In this way, we were forcing the fitting function to pass through these stars, i.e., approaching the constant value for cold giants. In a similar way, for the computation of the fitting functions of warm giants, we also created fake stars at $\theta = 1.10$ and $\theta = 1.13$, and we assigned their index value according to the fitting function for cool stars. A new set of random stars at $\theta = 0.92$ was introduced with the constant index value computed from hot stars. Finally, we used these fake stars, together with the real ones, to obtain the final fit for the warm giants.

We derived the local fitting functions computing a weighted least squares fit to the stars within each parameter range, with weights according to the inverse of the squared uncertainties of the indices for each individual star. Here we considered the nominal errors in the index measurements, using the uncertainties derived in Sect. 4.2 for the library stars, and the individual errors for each cluster quoted by Frogel et al. (2001) and Stephens & Frogel (2004). After the analysis of the residuals, it was necessary to repeat the fitting procedure with the inclusion of additional random uncertainties in some of the stars (see next section). The final fitting functions for each stellar parameter range are presented in Table 6. This table includes the functional forms of the fits, the significant coefficients and their corresponding formal errors, the typical index error for the $N$ stars employed in each interval ($\sigma^2_{\rm typ} = N/\sum_{i=1}^{N}\sigma_i^{-1}$), the unbiased residual variance of the fit ($\sigma^2_{\rm std}$) and the determination coefficient ($r^2$). Also the intersection regions are indicated and the procedure used for computing the index. We plot in Fig. 14 the fitting functions for giant and dwarf stars as a function of $\theta$ for several metallicities, as well as the simple fit for AGB stars. Figure 15 shows the final residuals ($\Delta D_{\rm CO} = D_{\rm CO\,obs} - D_{\rm CO\,pred}$) of the new CO index for the different groups of stars used for the computation of the fitting functions (stars observed at CAHA, stars observed at the TNG and cluster stars from previous works) as a function of the atmospheric parameters. As we expected, the residuals for each group of stars do not exhibit any systematic trend.

**Table 6.** Coefficients and statistical data for the local empirical fitting functions for the $D_{\rm CO}$ index in each range of stellar parameters.

| | | |
|---|---|---|
| **Hot dwarfs** | $0.38 < \theta < 0.90$ | $3.50 < \log g < 5.50$ |
| exponential fit | $N$ = 28 stars | $\sigma_{\rm typ}$ = 0.00913 |
| $c_0$ | 0.0499 ± 0.0011 | $\sigma_{\rm std}$ = 0.00557 |
| *Intersection* | Cosine-weighted mean | $0.80 < \theta < 0.90$ |
| **Cool dwarfs** | $0.80 < \theta < 1.50$ | $3.50 < \log g < 5.50$ |
| exponential fit | $N$ = 39 stars | $\sigma_{\rm typ}$ = 0.00748 |
| $c_0$ | −0.0292 ± 0.0330 | $\sigma_{\rm std}$ = 0.01254 |
| $\theta$ | 0.1006 ± 0.0329 | $r^2$ = 0.765 |
| [Fe/H] | 0.0174 ± 0.0067 | |
| *Intersection* | Cosine-weighted mean | $1.45 < \theta < 1.50$ |
| **Cold dwarfs** | $1.33 < \theta < 1.80$ | $3.50 < \log g < 5.50$ |
| exponential fit | $N$ = 7 stars | $\sigma_{\rm typ}$ = 0.00960 |
| $c_0$ | 0.1025 ± 0.0046 | $\sigma_{\rm std}$ = 0.01195 |
| **Hot giants** | $0.42 < \theta < 0.90$ | $-0.40 < \log g < 3.50$ |
| exponential fit | $N$ = 15 stars | $\sigma_{\rm typ}$ = 0.01954 |
| $c_0$ | 0.0459 ± 0.0010 | $\sigma_{\rm std}$ = 0.00398 |
| *Intersection* | Cosine-weighted mean | $0.90 < \theta < 0.93$ |
| **Warm giants** | $0.90 < \theta < 1.131$ | 0.13 $\log g < 3.5$ |
| exponential fit | $N$ = 63 stars | $\sigma_{\rm typ}$ = 0.00764 |
| $c_0$ | −0.3073 ± 0.0046 | $\sigma_{\rm std}$ = 0.00428 |
| $\theta$ | 0.3876 ± 0.0043 | $r^2$ = 0.982 |
| [Fe/H] | −0.1016 ± 0.0042 | |
| $\theta$[Fe/H] | 0.1072 ± 0.0039 | |
| [Fe/H]$^2$ | −0.0023 ± 0.0005 | |
| *Intersection* | Distance-weighed mean | $1.09 < \theta < 1.10$ |
| **Cool giants** | $1.10 < \theta < 1.60$ | $-0.34 < \log g < 3.41$ |
| exponential fit | $N$ = 167 stars | $\sigma_{\rm typ}$ = 0.01062 |
| $c_0$ | −0.5224 ± 0.0970 | $\sigma_{\rm std}$ = 0.00890 |
| $\theta$ | 0.8257 ± 0.1417 | $r^2$ = 0.958 |
| [Fe/H] | 0.0674 ± 0.0101 | |
| $\theta$[Fe/H] | −0.0444 ± 0.0065 | |
| $\theta^2$ | −0.2200 ± 0.0509 | |
| [Fe/H]$^2$ | −0.0023 ± 0.0014 | |
| *No intersection* | | |
| **Cold giants** | $1.55 < \theta < 2.03$ | $-0.07 < \log g < 3.50$ |
| exponential fit | $N$ = 7 stars | $\sigma_{\rm typ}$ = 0.02156 |
| $c_0$ | 0.2397 ± 0.0107 | $\sigma_{\rm std}$ = 0.02698 |
| **AGB stars** | $1.01 < \theta < 1.56$ | $-0.11 < \log g < 1.56$ |
| exponential fit | $N$ = 18 stars | $\sigma_{\rm typ}$ = 0.00612 |
| $c_0$ | −0.8893 ± 0.2198 | $\sigma_{\rm std}$ = 0.00892 |
| $\theta$ | 1.4950 ± 0.3610 | $r^2$ = 0.985 |
| $\theta^2$ | −0.4816 ± 0.1461 | |

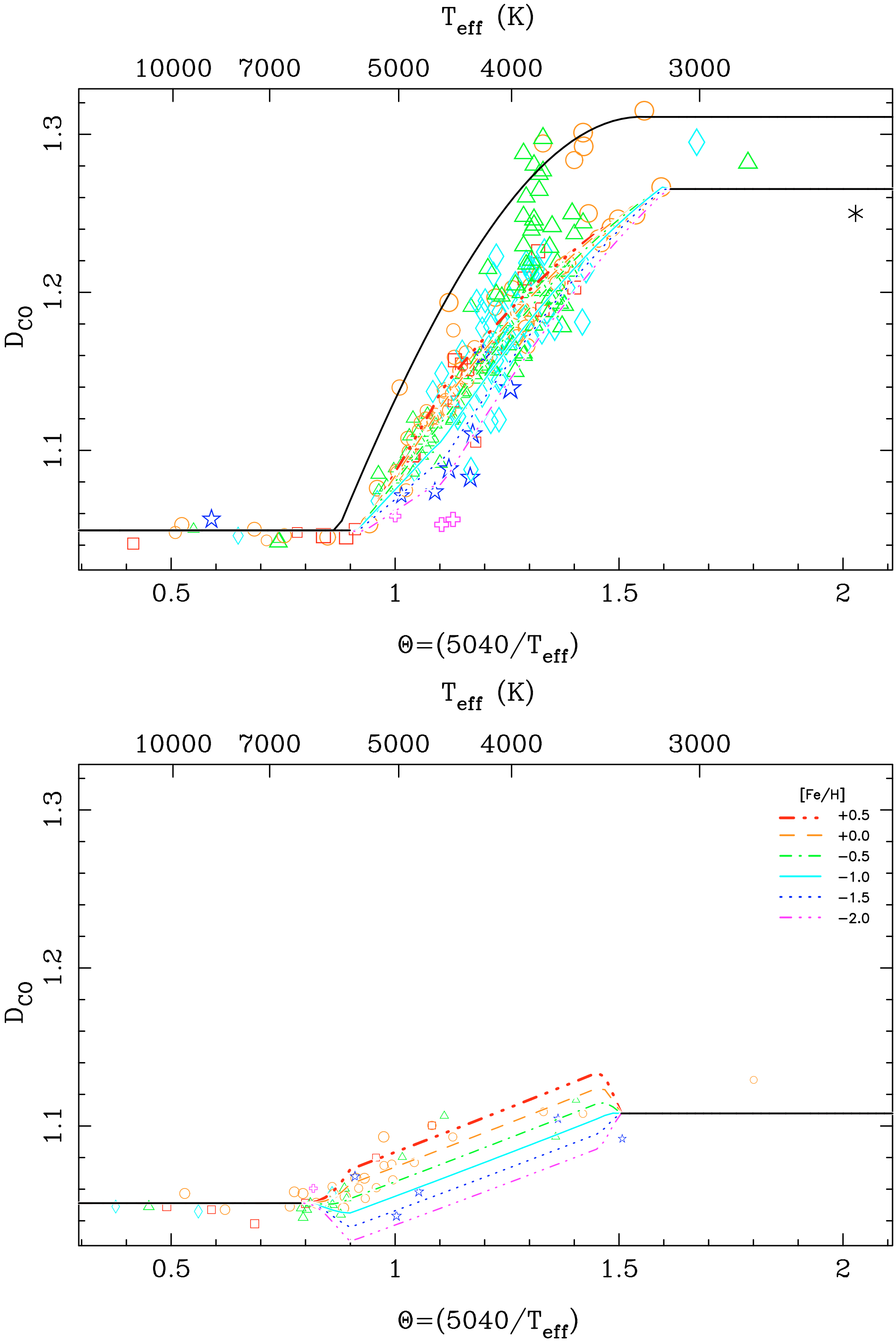

**Fig. 14.** Empirical fitting functions for the $D_{\rm CO}$ index for giants, including the fit for AGB stars (*top panel*) and dwarfs (*bottom panel*), computed as explained in the text. Symbol types and size mean metallicity and gravity, the same than in previous figures. The different lines represent the metallicities [Fe/H] = +0.5, +0.0, −0.5, −1.0, −1.5, and − 2.0, *from top to bottom*. The reduced scatter for $\theta \leq 0.9$ is due to the absence of CO absorptions for hot stars, as explained in the text.

Users interested in implementing these fitting functions into their population synthesis codes can make use of the FORTRAN subroutine available at the URL address `http://www.ucm.es/info/Astrof/ellipt/CO.html`

### 6.2.3. Residuals and error analysis

To explore the reliability of the fitting functions in more detail, we computed the unbiased residual standard deviation from the fits, $\sigma_{\rm std}$ = 0.0093, and the typical error in the measured

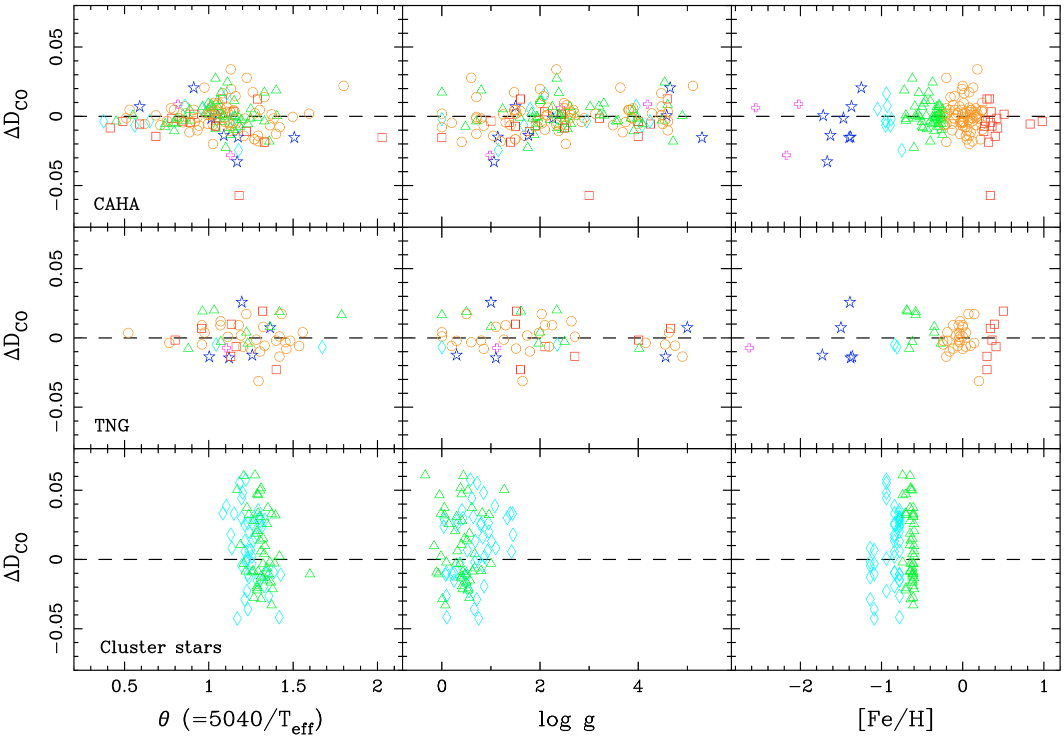

**Fig. 15.** Residuals of the derived fitting functions (observed minus derived) against the three input stellar atmospheric parameters for the stars observed at CAHA (*upper panels*) and TNG (*middle panels*). Cluster data from Frogel et al. (2001) and Stephens & Frogel (2004) are presented in *the lower panels*. Codes and relative sizes of the star symbols are explained in Figs. 1 and 13.

index, $\sigma_{\rm typ} = 0.0025$, for the stars employed in the computation of the global fitting functions derived above.

After the initial fit, we discovered that $\sigma_{\rm std}$ was larger than what should be expected uniquely from index uncertainties (see also the values of $\sigma_{\rm std}$ and $\sigma_{\rm typ}$ for different subgroups of stars in Table 7). Furthermore, a $F$ test of comparison of variances showed that $\sigma_{\rm std}$ was statistically larger than $\sigma_{\rm typ}$, leading to the introduction on an additional residual error ($\sigma^2_{\rm res} = \sigma^2_{\rm std} - \sigma^2_{\rm typ}$). Such residual error could be due to uncertainties in the input stellar atmospheric parameters, not included in the error budget so far. In order to check this, we computed how errors in the input stellar parameters translate into uncertainties in the predicted $D_{\rm CO}$. This depends both on the local functional form of the fitting function and on the atmospheric parameters range (e.g. hot stars have $T_{\rm eff}$ uncertainties larger than cooler stars). For each star of the sample, we derived the errors corresponding to the uncertainties in effective temperature ($\sigma_{T_{\rm eff}}$), gravity ($\sigma_{\log g}$) and metallicity ($\sigma_{\rm [Fe/H]}$). The effect of the uncertainties in the three stellar parameters were finally computed as $\sigma^2_{\rm par} = \sigma^2_{T_{\rm eff}} + \sigma^2_{\log g} + \sigma^2_{\rm [Fe/H]}$. Table 7 presents, summarized for the different stellar groups, all the error estimations already discussed. Finally, in the cases where the residual errors ($\sigma_{\rm res}$) were not explained by the uncertainties in the stellar parameters ($\sigma_{\rm par}$), an extra residual error was added to the original index error. At the end, no iterations were needed for the globular cluster stars and AGB stars, one iteration was required for the giants and two iterations for dwarfs (in any case, the additional error for dwarf stars is lower than the necessary for giants). The uncertainties of the final $D_{\rm CO}$ fitting functions are listed in Table 8. Although in this table $\sigma_{\rm std}$ is still larger than $\sigma_{\rm typ}$ for the four initial subgroups of stars analyzed in Table 7, both standard deviations are statistically comparable using the $F$ test of variances previously mentioned.

Finally, as the purpose of this paper is to predict reliable index values for any combination of input atmospheric parameters, we also computed the random errors in such predictions. These uncertainties are given in Table 9 for some representative values of input parameters.

## 7. Summary

The aim of this work was to obtain an accurate empirical calibration of the behavior of the CO feature at 2.3 μm for individual stars, with the purpose of making it possible to obtain reliable predictions for the CO strength for stellar populations in unresolved systems with a wide range of ages and metallicities. The main results of this work can be summarized as follows.

1. We present a new stellar library in the spectral region around the first CO bandhead at 2.3 μm. It consists of 220 stars with stellar atmospheric parameters in the range $2485 \leq T_{\rm eff} \leq 13404$ K, $-0.34 \leq \log g \leq 5.30$ dex, $-2.63 \leq {\rm [Fe/H]} \leq 0.98$ dex.
2. We define a new line-strength index for the first CO bandhead at 2.3 μm, $D_{\rm CO}$, less sensitive to spectral resolution, wavelength calibration, signal-to-noise ratio, and flux calibration than previous definitions.
3. We compute empirical fitting functions for the $D_{\rm CO}$ to parametrize the behavior of the CO feature as a function of the stellar atmospheric parameters. In this work we quantify the metallicity dependence for the first time.

We expect that the work presented in this paper will help researchers start exploiting in depth the so far poorly-explored and poorly-understood near-IR spectral region centered at 2.3 μm, since, as we have shown, the strong CO bandhead can be employed to extract useful physical information on composite stellar populations.

**Table 7.** Uncertainties of the initial $D_{\rm CO}$ fitting functions for different groups of stars and mean $D_{\rm CO}$ errors due to uncertainties in the input atmospheric parameters.

|  | $N$ | $\sigma_{\rm std}$ | $\sigma_{\rm typ}$ | $\sigma_{\rm res}$ | $\sigma_{T_{\rm eff}}$ | $\sigma_{\rm [Fe/H]}$ | $\sigma_{\rm par}$ |
|---|---|---|---|---|---|---|---|
| Field dwarfs | 54 | 0.0059 | 0.0017 | 0.0056 | 0.0010 | 0.0009 | 0.0014 |
| Field giants | 147 | 0.0108 | 0.0023 | 0.0105 | 0.0062 | 0.0019 | 0.0065 |
| Globular cluster stars | 85 | 0.0276 | 0.0236 |  | 0.0139 | 0.0010 | 0.0140 |
| AGB stars | 19 | 0.0115 | 0.0061 |  | 0.0097 | 0.0000 | 0.0097 |
| All | 305 | 0.0093 | 0.0025 |  | 0.0075 | 0.0014 | 0.0078 |

$N$: number of stars. $\sigma_{\rm std}$: unbiased residual standard deviation for the fit. $\sigma_{\rm typ}$: typical observational $\rm D_{CO}$ error for the subsample of stars. $\sigma_{\rm res}$: residual error. $\sigma_{T_{\rm eff}}$ and $\sigma_{\rm [Fe/H]}$: mean $D_{\rm CO}$ errors due to uncertainties in the input $T_{\rm eff}$ and [Fe/H] (no error due to uncertainties in the input $\log g$ is computed since the computed fitting functions do not require gravity terms). $\sigma_{\rm par}$: total error due to atmospheric parameters (quadratic sum of the previous errors). $\sigma_{\rm std}$ is not explained by the $\sigma_{\rm typ}$ and $\sigma_{\rm par}$ values for giants and dwarfs, and a residual error has been considered for these group of stars.

**Table 8.** Uncertainties of the final $\rm D_{CO}$ fitting functions for different groups of stars and same computed errors than in Table 7.

|  | $N$ | $\sigma_{\rm std}$ | $\sigma_{\rm typ}$ | $\sigma_{T_{\rm eff}}$ | $\sigma_{\rm [Fe/H]}$ | $\sigma_{\rm par}$ |
|---|---|---|---|---|---|---|
| Field dwarfs | 54 | 0.0086 | 0.0078 | 0.0010 | 0.0013 | 0.0017 |
| Field giants | 147 | 0.0123 | 0.0113 | 0.0062 | 0.0014 | 0.0064 |
| Globular cluster stars | 85 | 0.0252 | 0.0236 | 0.0135 | 0.0009 | 0.0135 |
| AGB stars | 19 | 0.0115 | 0.0061 | 0.0097 | 0.0000 | 0.0097 |
| All | 305 | 0.0130 | 0.0114 | 0.0074 | 0.0012 | 0.0076 |

**Table 9.** Absolute errors in the fitting functions predictions for different values of the atmospheric parameters.

|  |  |  | $\sigma[D_{\rm CO}]$ |  |
|---|---|---|---|---|
| $T_{\rm eff}$ | [Fe/H] | V | III | I |
| 6000 |  | 0.002 | 0.001 | 0.001 |
| 5500 | +0.5 | 0.010 | 0.002 | 0.002 |
| 5500 | +0.0 | 0.007 | 0.001 | 0.001 |
| 5500 | −1.0 | 0.006 | 0.001 | 0.001 |
| 5500 | −2.0 | 0.011 | 0.002 | 0.002 |
| 5000 | +0.5 | 0.010 | 0.001 | 0.001 |
| 5000 | +0.0 | 0.007 | 0.001 | 0.001 |
| 5000 | −1.0 | 0.005 | 0.001 | 0.001 |
| 5000 | −2.0 | 0.011 | 0.001 | 0.001 |
| 4500 | +0.5 | 0.011 | 0.004 | 0.004 |
| 4500 | +0.0 | 0.008 | 0.003 | 0.003 |
| 4500 | −1.0 | 0.007 | 0.003 | 0.003 |
| 4500 | −2.0 | 0.011 | 0.006 | 0.006 |
| 4000 | +0.5 | 0.014 | 0.003 | 0.003 |
| 4000 | +0.0 | 0.012 | 0.002 | 0.002 |
| 4000 | −1.0 | 0.011 | 0.003 | 0.003 |
| 4000 | −2.0 | 0.014 | 0.005 | 0.005 |
| 3500 | +0.5 | 0.018 | 0.003 | 0.007 |
| 3500 | +0.0 | 0.018 | 0.003 | 0.007 |
| 3500 | −1.0 | 0.018 | 0.003 | 0.007 |
| 3500 | −2.0 | 0.018 | 0.004 | 0.007 |
| 3000 |  | 0.005 | 0.014 | 0.014 |

Note: input $\log g$ values varying with effective temperature for dwarfs (V), giants (III) and supergiants (I) have been taken from Lang (1991).

*Acknowledgements.* This work was supported by the Spanish research projects AYA2006–14318, AYA2006–15698-C02-02, AYA2007–67752C03-03. E.M.Q. acknowledges the Spanish Ministry of Education and Science and the European Social Found for a Formación de Personal Investigador fellowship under the project AYA2003–01840. A.J.C. is a Juan de la Cierva Fellow of the Spanish Ministry of Education and Science. This research was supported by a Marie Curie Intra-European Fellowship within the 6th European Community Framework Program. Based on observations collected at the Centro Astronómico Hispano Alemán (CAHA) at Calar Alto, operated jointly by the Max-Planck Institut für Astronomie and the Instituto de Astrofísica de Andalucía (CSIC). Based on observations made with the Italian Telescopio Nazionale Galileo (TNG) operated on the island of La Palma by the Fundación Galileo Galilei of the INAF (Istituto Nazionale di Astrofisica) at the Spanish Observatorio del Roque de los Muchachos of the Instituto de Astrofísica de Canarias. This research made use of the SIMBAD database (operated at CDS, Strasbourg, France), the NASA's Astrophysiscs Data System Bibliographic Services, and the *Hipparcos* Input Catalogue. The authors are grateful to the allocation time committees for the generous concession of observing time. We finally thank the anonymous referee for very useful comments and suggestions.

## Appendix A: Stellar library and cluster stars

In Table A.1 we list the stars of the stellar library with their spectral type, $K$ magnitude, effective temperature and the associated uncertainty ($T_{\rm eff}$ and $\sigma[T_{\rm eff}]$), surface gravity and its uncertainty ($\log g$ and $\sigma[\log g]$), metallicity and its uncertainty ([Fe/H] and $\sigma$[Fe/H]), number of measurements ($N$), $D_{\rm CO}$ index and their error $\sigma[D_{\rm CO}]$. The stars observed at the TNG are labeled with a † in the index measurement.

In Table A.2 we list the cluster stars from Frogel et al. (2001) and Stephens & Frogel (2004) employed in the computation of the empirical fitting functions. We present the derived atmospheric parameters and their associated uncertainties, along with the $D_{\rm CO}$ index and error for each star.

In both tables, AGB stars are labeled with a ⋆ in the name of the star.

## References

Ali, B., Carr, J. S., Depoy, D. L., Frogel, J. A., & Sellgren, K. 1995, AJ, 110, 2415
Alonso, A., Arribas, S., & Martínez-Roger, C. 1999, A&AS, 140, 261
Baldwin, J. R., Frogel, J. A., & Persson, S. E. 1973, ApJ, 184, 427
Bendo, G. J., & Joseph, R. D. 2004, AJ, 127, 3338
Bruzual, G., & Charlot, S. 2003, MNRAS, 344, 1000
Cardiel, N. 1999, Ph.D. Thesis
Cardiel, N. 2007, in Highlights of Spanish astrophysics IV, ed. F. Figueras, J. Girart, M. Hernanz, & C. Jordi, CD-ROM

Cardiel, N., Gorgas, J., Cenarro, J., & Gonzalez, J. J. 1998, A&AS, 127, 597
Cardiel, N., Gorgas, J., Sánchez-Blázquez, P., et al. 2003, A&A, 409, 511
Carretta, E., & Gratton, R. G. 1997, A&AS, 121, 95
Cayrel de Strobel, G., Soubiran, C., & Ralite, N. 2001, A&A, 373, 159
Cenarro, A. J., Cardiel, N., Gorgas, J., et al. 2001a, MNRAS, 326, 959
Cenarro, A. J., Gorgas, J., Cardiel, N., et al. 2001b, MNRAS, 326, 981
Cenarro, A. J., Gorgas, J., Cardiel, N., Vazdekis, A., & Peletier, R. F. 2002, MNRAS, 329, 863
Cenarro, A. J., Peletier, R. F., Sánchez-Blázquez, P., et al. 2007, MNRAS, 374, 664
Crampin, J., & Hoyle, F. 1961, MNRAS, 122, 27
Cushing, M. C., Rayner, J. T., & Vacca, W. D. 2005, ApJ, 623, 1115
Davidge, T. J., Beck, T. L., & McGregor, P. J. 2008, ApJ, 677, 238
Davidge, T. J. & Jensen, J. B. 2007, AJ, 133, 576
Doyon, R., Joseph, R. D., & Wright, G. S. 1994, ApJ, 421, 101
Förster Schreiber, N. M. 2000, AJ, 120, 2089
Frogel, J. A., Becklin, E. E., Neugebauer, G., et al. 1975, ApJ, 195, L15
Frogel, J. A., Kuchinski, L. E., & Tiede, G. P. 1995, AJ, 109, 1154
Frogel, J. A., Persson, S. E., & Cohen, J. G. 1980, ApJ, 240, 785
Frogel, J. A., Persson, S. E., Matthews, K., & Aaronson, M. 1978, ApJ, 220, 75
Frogel, J. A., Stephens, A., Ramírez, S., & DePoy, D. L. 2001, AJ, 122, 1896
Girardi, L., Bressan, A., Bertelli, G., & Chiosi, C. 2000, A&AS, 141, 371
Goldader, J. D., Joseph, R. D., Doyon, R., & Sanders, D. B. 1997, ApJ, 474, 104
Gorgas, J., Cardiel, N., Pedraz, S., & González, J. J. 1999, A&AS, 139, 29
Gorgas, J., Faber, S. M., Burstein, D., et al. 1993, ApJS, 86, 153
Hanson, M. M., Conti, P. S., & Rieke, M. J. 1996, ApJS, 107, 281
Hanson, M. M., Kudritzki, R.-P., Kenworthy, M. A., Puls, J., & Tokunaga, A. T. 2005, ApJS, 161, 154
Harris, W. E. 1996, AJ, 112, 1487
Hill, T. L., Heisler, C. A., Sutherland, R., & Hunstead, R. W. 1999, AJ, 117, 111
Hopp, U., & Fernández, M. 2002, Calar Alto Newsletter, 4
Ivanov, V. D., Rieke, G. H., Groppi, C. E., et al. 2000, ApJ, 545, 190
Ivanov, V. D., Rieke, M. J., Engelbracht, C. W., et al. 2004, ApJS, 151, 387
James, P. A., & Mobasher, B. 1999, MNRAS, 306, 199
James, P. A., & Seigar, M. S. 1999, A&A, 350, 791
Johnson, H. J., & Mendez, M. E. 1970, AJ, 75, 785
Kleinmann, S. G., & Hall, D. N. B. 1986, ApJS, 62, 501
Kuchinski, L. E., & Frogel, J. A. 1995, AJ, 110, 2844
Kuchinski, L. E., Frogel, J. A., Terndrup, D. M., & Persson, S. E. 1995, AJ, 109, 1131
Lançon, A., & Rocca-Volmerange, B. 1992, A&AS, 96, 593
Lançon, A., & Wood, P. R. 2000, A&AS, 146, 217
Lang, L. 1991, Astrophysical Data: Planets and Stars (Springer-Verlag), 1
Lejeune, T., Cuisinier, F., & Buser, R. 1997, A&AS, 125, 229
Lejeune, T., Cuisinier, F., & Buser, R. 1998, A&AS, 130, 65
Livingston, W., & Wallace, L. 1991, An atlas of the solar spectrum in the infrared from 1850 to 9000 cm$^{-1}$, 1.1 to 5.4 micrometer, NSO Technical Report, Tucson: National Solar Observatory, National Optical Astronomy Observatory
Mannucci, F., Basile, F., Poggianti, B. M., et al. 2001, MNRAS, 326, 745
Maraston, C. 2005, MNRAS, 362, 799
Mayya, Y. D. 1997, ApJ, 482, L149
McWilliam, A., & Lambert, D. L. 1984, PASP, 96, 882
Mieske, S., & Kroupa, P. 2008, ApJ, 677, 276
Mobasher, B., & James, P. A. 1996, MNRAS, 280, 895
Mobasher, B., & James, P. A. 2000, MNRAS, 316, 507
Oliva, E., & Origlia, L. 1992, A&A, 254, 466
Origlia, L., Moorwood, A. F. M., & Oliva, E. 1993, A&A, 280, 536
Origlia, L., & Oliva, E. 2000, A&A, 357, 61
Puxley, P. J., Doyon, R., & Ward, M. J. 1997, ApJ, 476, 120
Ramirez, S. V., Depoy, D. L., Frogel, J. A., Sellgren, K., & Blum, R. D. 1997, AJ, 113, 1411
Ranada, A. C., Singh, H. P., Gupta, R., & Ashok, N. M. 2007, Bulletin of the Astronomical Society of India, 35, 87
Ridgway, S. E., Wynn-Williams, C. G., & Becklin, E. E. 1994, ApJ, 428, 609
Riffel, R., Pastoriza, M. G., Rodríguez-Ardila, A., & Maraston, C. 2007, ApJ, 659, L103
Rousselot, P., Lidman, C., Cuby, J.-G., Moreels, G., & Monnet, G. 2000, A&A, 354, 1134
Rutledge, G. A., Hesser, J. E., & Stetson, P. B. 1997, PASP, 109, 907
Sánchez-Blázquez, P., Peletier, R. F., Jiménez-Vicente, J., et al. 2006, MNRAS, 371, 703
Shier, L. M., Rieke, M. J., & Rieke, G. H. 1996, ApJ, 470, 222
Silva, D. R., Kuntschner, H., & Lyubenova, M. 2008, ApJ, 674, 194
Stephens, A. W., & Frogel, J. A. 2004, AJ, 127, 925
Terndrup, D. M., Frogel, J. A., & Whitford, A. E. 1991, ApJ, 378, 742
Tinsley, B. M. 1972, ApJ, 178, 319
Tinsley, B. M. 1978, ApJ, 222, 14
Tinsley, B. M. 1980, Fundamentals of Cosmic Phys., 5, 287
Turon, C., Crézé, M., Egret, D., & et al. 1992, The HIPPARCOS input catalogue (ESA Special Publication), 1136
Vanzi, L., & Rieke, G. H. 1997, ApJ, 479, 694
Vazdekis, A., Cenarro, A. J., Gorgas, J., Cardiel, N., & Peletier, R. F. 2003, MNRAS, 340, 1317
Wallace, L., & Hinkle, K. 1996, ApJS, 107, 312
Wallace, L., & Hinkle, K. 1997, ApJS, 111, 445
Worthey, G. 1994, ApJS, 95, 107
Worthey, G., Faber, S. M., Gonzalez, J. J., & Burstein, D. 1994, ApJS, 94, 687
Zinn, R., & West, M. J. 1984, ApJS, 55, 45

**Table A.1.** Stellar library used in the fitting function procedure.

| Name | Spectral type | $K$ (mag) | $T_{\rm eff}$ (K) | $\sigma[T_{\rm eff}]$ | $\log g$ (dex) | $\sigma[\log g]$ | [Fe/H] (dex) | $\sigma$[Fe/H] | $N$ | $D_{\rm CO}$ | $\sigma[D_{\rm CO}]$ |
|---|---|---|---|---|---|---|---|---|---|---|---|
| BD+012916 | KIIvw | +6.47 | 4150 | 60.9 | 0.10 | 0.18 | −1.99 | 0.09 | 2 | 1.092 | 0.010 |
| BD+233130 | G0 | +6.95 | 5039 | 75.0 | 2.42 | 0.40 | −2.55 | 0.15 | 2 | 1.058 | 0.012 |
| BD+442051 | M2V | +4.77 | 3696 | 60.9 | 5.00 | 0.18 | −1.50 | 0.09 | 4 | $1.105^{\dagger}$ | 0.010 |
| G171-010 | M6eV | +5.93 | 2799 | 60.9 | 5.12 | 0.18 | – | 0.09 | 2 | 1.129 | 0.009 |
| HD 001326B | M6V | +5.95 | 3344 | 60.9 | 5.30 | 0.18 | −1.40 | 0.09 | 2 | 1.092 | 0.009 |
| HD 004628 | K2V | +3.68 | 4960 | 75.0 | 4.60 | 0.40 | −0.29 | 0.15 | 2 | 1.080 | 0.009 |
| HD 010307 | G2V | +3.57 | 5838 | 60.9 | 4.28 | 0.18 | +0.03 | 0.09 | 2 | 1.057 | 0.009 |
| HD 013043 | G2V | +5.38 | 5695 | 60.9 | 3.68 | 0.18 | +0.10 | 0.09 | 3 | 1.048 | 0.009 |
| HD 013555 | F5V | +4.12 | 6378 | 60.9 | 4.01 | 0.18 | −0.35 | 0.09 | 3 | 1.048 | 0.009 |
| HD 014221 | F4V | +5.25 | 6342 | 60.9 | 3.91 | 0.18 | −0.35 | 0.09 | 3 | 1.042 | 0.009 |
| HD 014662 | F7Ib | +4.18 | 5933 | 117.6 | 1.30 | 0.21 | −0.03 | 0.09 | 3 | 1.045 | 0.011 |
| HD 015596 | G5III-IV | +3.86 | 4755 | 75.0 | 2.50 | 0.40 | −0.70 | 0.15 | 3 | 1.097 | 0.011 |
| HD 015798 | F5V | +3.47 | 6345 | 60.9 | 3.85 | 0.18 | −0.16 | 0.09 | 3 | 1.057 | 0.009 |
| HD 016901 | G0Ib-II | +3.56 | 5345 | 117.6 | 0.85 | 0.21 | +0.00 | 0.09 | 3 | 1.053 | 0.010 |
| HD 017361 | K1.5III | +2.09 | 4600 | 60.9 | 2.85 | 0.18 | −0.02 | 0.09 | 3 | 1.120 | 0.011 |
| HD 017382 | K1V | +5.61 | 5065 | 75.0 | 4.50 | 0.40 | −0.13 | 0.15 | 3 | 1.066 | 0.009 |
| HD 020619 | G0 | +5.46 | 5652 | 60.9 | 4.48 | 0.18 | −0.26 | 0.09 | 3 | 1.054 | 0.010 |
| HD 020893 | K3III | +2.19 | 4340 | 60.9 | 2.04 | 0.18 | +0.08 | 0.09 | 3 | 1.146 | 0.011 |
| HD 021017 | K4III | +2.88 | 4410 | 60.9 | 2.36 | 0.18 | +0.00 | 0.09 | 3 | 1.138 | 0.011 |
| HD 021197 | K5V | +5.12 | 4657 | 117.6 | 4.59 | 0.21 | +0.33 | 0.10 | 3 | 1.100 | 0.010 |
| HD 021910 | G8III-IV | +4.99 | 4582 | 60.9 | 1.75 | 0.18 | −0.60 | 0.09 | 3 | 1.092 | 0.011 |
| HD 023841 | K1III | +3.80 | 4279 | 60.9 | 1.67 | 0.21 | −0.95 | 0.09 | 2 | 1.130 | 0.012 |
| HD 025329 | K1Vsb | +6.20 | 4787 | 75.0 | 4.58 | 0.40 | −1.72 | 0.15 | 2 | 1.058 | 0.009 |
| HD 026297 | G5-6IVw | +6.12 | 4316 | 75.0 | 1.06 | 0.40 | −1.67 | 0.15 | 3 | 1.083 | 0.011 |
| HD 026322 | F2IV-V | +4.48 | 7072 | 60.9 | 3.49 | 0.18 | +0.16 | 0.09 | 3 | 1.043 | 0.011 |
| HD 026846 | K3III | +2.27 | 4541 | 60.9 | 2.62 | 0.18 | +0.15 | 0.09 | 2 | 1.137 | 0.011 |
| HD 027371 | K0III | +1.51 | 4271 | 60.9 | 3.00 | 0.18 | +0.34 | 0.09 | 2 | 1.105 | 0.011 |
| HD 027819 | A7V | +4.41 | 8129 | 60.9 | 4.00 | 0.18 | −0.20 | 0.09 | 3 | 1.047 | 0.009 |
| HD 028305 | G9.5III | +1.42 | 4846 | 60.9 | 2.68 | 0.18 | +0.11 | 0.09 | 3 | 1.106 | 0.011 |
| HD 029139 | K5III | −3.04 | 3910 | 75.0 | 1.59 | 0.40 | −0.34 | 0.15 | 3 | 1.188 | 0.011 |
| HD 030959 | M3Svar | −0.66 | 3451 | 117.6 | 0.80 | 0.21 | −0.15 | 0.10 | 3 | 1.220 | 0.010 |
| HD 031295 | A0V | +4.41 | 8991 | 117.6 | 4.08 | 0.21 | −0.89 | 0.10 | 3 | 1.046 | 0.009 |
| HD 031767 | K2II | +1.34 | 4120 | 60.9 | 1.78 | 0.18 | +0.26 | 0.09 | 3 | 1.164 | 0.011 |
| HD 032147 | K3V | +3.71 | 4658 | 100.0 | 4.47 | 0.50 | +0.02 | 0.30 | 3 | 1.100 | 0.009 |
| HD 035155 | S?I | +2.13 | 3600 | 117.6 | 0.80 | 0.21 | −0.72 | 0.10 | 2 | 1.237 | 0.012 |
| HD 035369 | G8III | +2.06 | 4863 | 75.0 | 2.50 | 0.40 | −0.26 | 0.15 | 3 | 1.097 | 0.011 |
| HD 035601$^{\star}$ | M1.5Ia | +1.66 | 3550 | 60.9 | 0.00 | 0.18 | +0.00 | 0.09 | 4 | $1.301^{\dagger}$ | 0.010 |
| HD 036003 | K5V | +4.88 | 4465 | 60.9 | 4.61 | 0.18 | +0.09 | 0.10 | 3 | 1.093 | 0.009 |
| HD 036395 | M1V | +4.00 | 3590 | 60.9 | 4.90 | 0.21 | −0.45 | 0.09 | 3 | 1.116 | 0.009 |
| HD 037160 | G8III-IV | +1.80 | 4668 | 75.0 | 2.46 | 0.40 | −0.50 | 0.15 | 3 | 1.105 | 0.011 |
| HD 037536$^{\star}$ | M2Iabs | +0.97 | 3789 | 117.6 | 0.70 | 0.21 | −0.15 | 0.10 | 3 | 1.294 | 0.010 |
| HD 037828 | K0 | +4.06 | 4296 | 75.0 | 1.14 | 0.40 | −1.38 | 0.15 | 3 | 1.110 | 0.011 |
| HD 037984 | K1III | +2.21 | 4404 | 60.9 | 2.45 | 0.18 | −0.26 | 0.09 | 3 | 1.129 | 0.011 |
| HD 038656 | G8III | +2.24 | 4928 | 60.9 | 2.52 | 0.18 | −0.22 | 0.09 | 3 | 1.085 | 0.011 |
| HD 039364 | G8III/IV | +1.40 | 4550 | 60.9 | 2.10 | 0.18 | −0.94 | 0.09 | 3 | 1.125 | 0.012 |
| HD 039801$^{\star}$ | M2Iab | −3.56 | 3547 | 60.9 | 0.00 | 0.21 | +0.03 | 0.10 | 3 | 1.292 | 0.010 |
| HD 040657 | K1.5III | +1.64 | 4370 | 60.9 | 2.42 | 0.18 | −0.58 | 0.09 | 3 | 1.136 | 0.011 |
| HD 041597 | G8III | +2.89 | 4700 | 75.0 | 2.38 | 0.40 | −0.54 | 0.15 | 3 | 1.123 | 0.011 |
| HD 041636 | G9III | +3.97 | 4709 | 60.9 | 2.50 | 0.18 | −0.20 | 0.09 | 3 | 1.116 | 0.011 |
| HD 042474$^{\star}$ | M2Iabpe... | +1.85 | 3789 | 117.6 | 0.70 | 0.21 | −0.36 | 0.10 | 2 | 1.277 | 0.010 |
| HD 042543$^{\star}$ | M1Ia-ab | +0.80 | 3789 | 117.6 | 0.00 | 0.21 | −0.42 | 0.10 | 3 | 1.298 | 0.010 |
| HD 044007 | G5IVw | +6.97 | 4969 | 75.0 | 2.26 | 0.40 | −1.47 | 0.15 | 3 | 1.071 | 0.012 |
| HD 044889 | K0I | +3.60 | 3775 | 117.6 | 0.40 | 0.21 | −0.20 | 0.10 | 4 | 1.186 | 0.014 |
| HD 045829$^{\star}$ | K0Iab | +3.35 | 4500 | 117.6 | 0.20 | 0.21 | −0.01 | 0.09 | 2 | 1.194 | 0.010 |
| HD 047914 | K5III | +1.70 | 3962 | 60.9 | 1.50 | 0.18 | +0.05 | 0.09 | 3 | 1.172 | 0.011 |
| HD 048329 | G8Ib | +0.12 | 4150 | 60.9 | 0.80 | 0.21 | +0.20 | 0.09 | 2 | 1.170 | 0.012 |
| HD 048433 | K1III | +1.93 | 4460 | 100.0 | 1.88 | 0.50 | −0.25 | 0.30 | 3 | 1.120 | 0.011 |
| HD 048565 | F8 | +5.80 | 5929 | 60.9 | 3.59 | 0.18 | −0.70 | 0.09 | 3 | 1.048 | 0.009 |
| HD 049161 | K4III | +1.58 | 4176 | 60.9 | 1.69 | 0.18 | +0.08 | 0.09 | 3 | 1.153 | 0.011 |
| HD 049331$^{\star}$ | M1II | +0.56 | 3600 | 117.6 | 0.70 | 0.21 | −0.03 | 0.10 | 2 | 1.284 | 0.010 |
| HD 052005 | K4Iab | +2.10 | 4117 | 60.9 | 0.60 | 0.18 | −0.20 | 0.09 | 2 | 1.197 | 0.011 |
| HD 052973 | G0Ibvar | +2.13 | 5659 | 117.6 | 1.37 | 0.21 | +0.34 | 0.10 | 3 | 1.045 | 0.010 |
| HD 054810 | K0III | +2.44 | 4697 | 60.9 | 2.35 | 0.18 | −0.30 | 0.09 | 2 | 1.111 | 0.011 |
| HD 057264 | G8III | +2.75 | 4620 | 60.9 | 2.72 | 0.18 | −0.33 | 0.09 | 3 | 1.116 | 0.011 |
| HD 058207 | K0III | +1.56 | 4788 | 60.9 | 2.55 | 0.18 | −0.12 | 0.09 | 3 | 1.113 | 0.011 |
| HD 058521$^{\star}$ | M5Ib-IIvar | −0.68 | 3238 | 60.9 | 0.00 | 0.18 | −0.19 | 0.09 | 4 | $1.315^{\dagger}$ | 0.010 |

**Table A.1.** continued.

| Name | Spectral type | $K$ (mag) | $T_{\rm eff}$ (K) | $\sigma[T_{\rm eff}]$ | $\log g$ (dex) | $\sigma[\log g]$ | [Fe/H] (dex) | $\sigma$[Fe/H] | $N$ | $D_{\rm CO}$ | $\sigma[D_{\rm CO}]$ |
|---|---|---|---|---|---|---|---|---|---|---|---|
| HD 060179 | A1V | +1.64 | 10286 | 117.6 | 4.00 | 0.21 | +0.98 | 0.10 | 2 | 1.049 | 0.009 |
| HD 060522 | M0III-IIIb | +0.23 | 3899 | 60.9 | 1.20 | 0.18 | +0.12 | 0.09 | 2 | 1.177 | 0.015 |
| HD 061064 | F6III | +4.21 | 6449 | 60.9 | 3.21 | 0.21 | +0.42 | 0.09 | 3 | 1.048 | 0.011 |
| HD 061603 | K5III | +2.17 | 3870 | 60.9 | 1.50 | 0.18 | +0.24 | 0.09 | 3 | 1.204 | 0.012 |
| HD 061606 | K2V | +4.88 | 4833 | 117.6 | 4.55 | 0.21 | +0.07 | 0.09 | 3 | 1.077 | 0.009 |
| HD 061772 | K3III | +1.33 | 3995 | 60.9 | 1.47 | 0.18 | +0.08 | 0.09 | 2 | 1.203 | 0.011 |
| HD 062345 | G8IIIa | +1.52 | 5017 | 60.9 | 2.63 | 0.18 | −0.08 | 0.09 | 3 | 1.086 | 0.011 |
| HD 062721 | K5III | +1.23 | 3954 | 60.9 | 1.52 | 0.18 | −0.22 | 0.09 | 2 | 1.188 | 0.011 |
| HD 063352 | K0III | +2.87 | 4226 | 60.9 | 2.20 | 0.18 | −0.31 | 0.09 | 3 | 1.153 | 0.011 |
| HD 063791 | G0 | +5.42 | 4629 | 75.0 | 1.76 | 0.40 | −1.63 | 0.15 | 2 | 1.074 | 0.011 |
| HD 064332 | S?I | +2.30 | 3500 | 117.6 | 0.50 | 0.21 | −0.34 | 0.10 | 2 | 1.242 | 0.010 |
| HD 065714 | G8III | +3.91 | 4840 | 60.9 | 1.50 | 0.18 | +0.27 | 0.09 | 2 | 1.097 | 0.012 |
| HD 066141 | K2III | +1.44 | 4258 | 60.9 | 1.90 | 0.18 | −0.30 | 0.09 | 3 | 1.145 | 0.011 |
| HD 068284 | F8V | +6.26 | 5860 | 60.9 | 3.98 | 0.18 | −0.57 | 0.09 | 3 | 1.050 | 0.009 |
| HD 069267 | K4III | +0.19 | 4043 | 60.9 | 1.51 | 0.18 | −0.12 | 0.09 | 4 | $1.170^{\dagger}$ | 0.011 |
| HD 070272 | K5III | +0.37 | 3900 | 60.9 | 1.05 | 0.18 | +0.04 | 0.09 | 3 | 1.180 | 0.011 |
| HD 072184 | K2III | +3.50 | 4624 | 60.9 | 2.61 | 0.18 | +0.12 | 0.09 | 2 | 1.123 | 0.013 |
| HD 072324 | G9III | +3.97 | 4887 | 60.9 | 2.13 | 0.18 | +0.16 | 0.09 | 3 | 1.099 | 0.011 |
| HD 072905 | G1.5Vb | +4.17 | 5864 | 60.9 | 4.48 | 0.18 | −0.04 | 0.09 | 3 | 1.061 | 0.010 |
| HD 073394 | G5IIIw | +4.95 | 4500 | 60.9 | 1.10 | 0.18 | −1.38 | 0.09 | 4 | $1.088^{\dagger}$ | 0.011 |
| HD 073593 | G8IV | +2.96 | 4717 | 60.9 | 2.25 | 0.18 | −0.12 | 0.09 | 4 | $1.120^{\dagger}$ | 0.011 |
| HD 074000 | F6VI | +8.39 | 6166 | 60.9 | 4.19 | 0.18 | −2.02 | 0.09 | 2 | 1.061 | 0.010 |
| HD 074395 | G2Iab | +2.85 | 5250 | 117.6 | 1.30 | 0.21 | −0.05 | 0.09 | 4 | $1.076^{\dagger}$ | 0.010 |
| HD 074442 | K0III | +1.56 | 4657 | 60.9 | 2.51 | 0.18 | −0.06 | 0.09 | 3 | 1.120 | 0.011 |
| HD 075732 | G8V | +4.01 | 5079 | 75.0 | 4.48 | 0.40 | +0.16 | 0.15 | 3 | 1.076 | 0.009 |
| HD 076813 | G9III | +3.15 | 6072 | 117.6 | 4.20 | 0.21 | −0.82 | 0.10 | 4 | $1.082^{\dagger}$ | 0.010 |
| HD 076932 | F7-8IV-V | +4.36 | 5866 | 100.0 | 3.96 | 0.50 | −0.93 | 0.30 | 3 | 1.057 | 0.009 |
| HD 078712 | M6SI | −1.87 | 3202 | 60.9 | 0.00 | 0.18 | −0.11 | 0.09 | 4 | $1.216^{\dagger}$ | 0.010 |
| HD 078732 | G8II | +3.20 | 4900 | 117.6 | 2.00 | 0.21 | +0.24 | 0.10 | 8 | 1.108 | 0.011 |
| HD 079211 | M0V | +4.14 | 3710 | 60.9 | 4.71 | 0.18 | −0.40 | 0.10 | 3 | 1.093 | 0.010 |
| HD 079452 | G6III | +3.86 | 4829 | 60.9 | 2.35 | 0.18 | −0.84 | 0.09 | 4 | $1.086^{\dagger}$ | 0.012 |
| HD 081192 | G7III | +4.11 | 4705 | 75.0 | 2.50 | 0.40 | −0.62 | 0.15 | 4 | $1.101^{\dagger}$ | 0.011 |
| HD 082074 | G6IV | +4.15 | 5055 | 117.6 | 3.30 | 0.21 | −0.48 | 0.10 | 2 | 1.088 | 0.011 |
| HD 082885 | G8IV-V | +3.69 | 5488 | 60.9 | 4.61 | 0.18 | +0.00 | 0.09 | 2 | 1.061 | 0.009 |
| HD 083425 | K3III | +1.58 | 4120 | 60.9 | 2.00 | 0.18 | −0.35 | 0.09 | 4 | $1.170^{\dagger}$ | 0.011 |
| HD 083618 | K3III | +0.87 | 4231 | 60.9 | 1.74 | 0.18 | −0.08 | 0.09 | 4 | $1.161^{\dagger}$ | 0.011 |
| HD 083632 | K2III | +4.72 | 4214 | 60.9 | 1.00 | 0.21 | −1.39 | 0.09 | 4 | $1.160^{\dagger}$ | 0.011 |
| HD 085235 | A3IV | +4.37 | 11200 | 117.6 | 3.55 | 0.21 | −0.40 | 0.10 | 3 | 1.049 | 0.009 |
| HD 085503 | K0III | +1.36 | 4472 | 75.0 | 2.33 | 0.40 | +0.23 | 0.15 | 3 | 1.136 | 0.011 |
| HD 085773 | G:w?I | +7.95 | 4463 | 60.9 | 0.98 | 0.18 | −2.17 | 0.09 | 1 | 1.056 | 0.014 |
| HD 087737 | A0Ib | +3.29 | 9625 | 60.9 | 1.98 | 0.21 | −0.04 | 0.10 | 4 | $1.053^{\dagger}$ | 0.010 |
| HD 087822 | F4V | +5.13 | 6590 | 60.9 | 4.15 | 0.18 | +0.14 | 0.09 | 4 | $1.049^{\dagger}$ | 0.009 |
| HD 089484 | K1IIIb | −0.81 | 4470 | 60.9 | 2.35 | 0.18 | −0.49 | 0.09 | 3 | 1.119 | 0.011 |
| HD 089822B | A0sp?III | +3.39 | 5538 | 117.6 | 2.44 | 0.21 | +0.51 | 0.10 | 2 | 1.050 | 0.010 |
| HD 092523 | K3III | +1.55 | 4090 | 60.9 | 1.96 | 0.18 | −0.38 | 0.09 | 2 | 1.163 | 0.011 |
| HD 093487 | F8 | +6.76 | 5250 | 60.9 | 1.80 | 0.18 | −1.05 | 0.09 | 2 | 1.068 | 0.012 |
| HD 095578 | M0III | +0.80 | 3700 | 60.9 | 1.40 | 0.18 | −0.23 | 0.09 | 2 | 1.206 | 0.011 |
| HD 095735 | M2V | +3.25 | 3551 | 60.9 | 4.90 | 0.21 | −0.20 | 0.09 | 8 | $1.108^{\dagger}$ | 0.009 |
| HD 096360 | M?I | +2.76 | 3550 | 117.6 | 0.50 | 0.21 | −0.58 | 0.10 | 4 | $1.244^{\dagger}$ | 0.012 |
| HD 097907 | K3III | +2.43 | 4351 | 60.9 | 2.07 | 0.18 | −0.10 | 0.09 | 2 | 1.162 | 0.011 |
| HD 099648 | G8II-III | +2.83 | 4850 | 117.6 | 1.90 | 0.21 | +0.36 | 0.10 | 3 | 1.097 | 0.011 |
| HD 099998 | K4III | +1.24 | 3863 | 60.9 | 1.79 | 0.18 | −0.16 | 0.09 | 4 | $1.186^{\dagger}$ | 0.011 |
| HD 101501 | G8Vvar | +3.58 | 5401 | 60.9 | 4.60 | 0.18 | −0.13 | 0.09 | 3 | 1.054 | 0.009 |
| HD 102224 | K0III | +0.98 | 4383 | 75.0 | 2.02 | 0.40 | −0.46 | 0.15 | 2 | 1.148 | 0.011 |
| HD 102328 | K3III | +2.63 | 4390 | 60.9 | 2.09 | 0.18 | +0.35 | 0.09 | 2 | 1.155 | 0.011 |
| HD 103095 | G8Vp | +4.37 | 5025 | 60.9 | 4.56 | 0.18 | −1.36 | 0.09 | 4 | $1.043^{\dagger}$ | 0.002 |
| HD 103877 | AmV | +5.88 | 7341 | 117.6 | 4.00 | 0.21 | +0.40 | 0.09 | 1 | 1.038 | 0.009 |
| HD 104307 | K2III | +3.68 | 4451 | 117.6 | 2.00 | 0.21 | −0.01 | 0.10 | 2 | 1.159 | 0.012 |
| HD 105262 | B9 | +6.75 | 8542 | 117.6 | 1.50 | 0.21 | −1.37 | 0.10 | 2 | 1.056 | 0.010 |
| HD 107213 | F8Vs | +5.13 | 6298 | 60.9 | 4.01 | 0.18 | +0.36 | 0.09 | 4 | $1.051^{\dagger}$ | 0.009 |
| HD 110014 | K2III | +2.01 | 4399 | 60.9 | 1.47 | 0.18 | +0.10 | 0.09 | 3 | 1.151 | 0.011 |
| HD 111631 | M0.5V | +4.88 | 3785 | 60.9 | 4.75 | 0.21 | +0.10 | 0.09 | 4 | $1.109^{\dagger}$ | 0.011 |
| HD 113092 | K2III | +2.11 | 4283 | 60.9 | 1.95 | 0.18 | −0.37 | 0.09 | 3 | 1.148 | 0.011 |
| HD 113285 | M8III | −1.06 | 2485 | 117.6 | 0.00 | 0.18 | – | – | 5 | 1.250 | 0.012 |
| HD 114038 | K1III | +2.72 | 4530 | 60.9 | 2.71 | 0.18 | −0.04 | 0.09 | 4 | $1.132^{\dagger}$ | 0.011 |

**Table A.1.** continued.

| Name | Spectral type | $K$ (mag) | $T_{\rm eff}$ (K) | $\sigma[T_{\rm eff}]$ | $\log g$ (dex) | $\sigma[\log g]$ | [Fe/H] (dex) | $\sigma$[Fe/H] | $N$ | $D_{\rm CO}$ | $\sigma[D_{\rm CO}]$ |
|---|---|---|---|---|---|---|---|---|---|---|---|
| HD 114095 | G5 | +5.88 | 4650 | 60.9 | 2.40 | 0.18 | −0.70 | 0.09 | 2 | 1.108 | 0.011 |
| HD 114330 | AV1 | +4.30 | 9509 | 117.6 | 3.80 | 0.21 | −0.01 | 0.10 | 2 | 1.057 | 0.011 |
| HD 114946 | G6V | +3.11 | 5171 | 60.9 | 3.64 | 0.18 | +0.13 | 0.09 | 3 | 1.093 | 0.010 |
| HD 114961$^{\star}$ | M7III | +1.50 | 3012 | 112.8 | 0.00 | 0.18 | −0.81 | 0.09 | 8 | $1.295^{\dagger}$ | 0.010 |
| HD 117176 | G5V | +3.50 | 5525 | 60.9 | 3.81 | 0.18 | −0.10 | 0.09 | 2 | 1.067 | 0.009 |
| HD 117876 | G8III | +3.87 | 4782 | 75.0 | 2.25 | 0.40 | −0.50 | 0.15 | 3 | 1.106 | 0.012 |
| HD 119228 | M2III | +0.33 | 3600 | 60.9 | 1.60 | 0.18 | +0.30 | 0.09 | 8 | $1.203^{\dagger}$ | 0.011 |
| HD 119667 | K5 | +4.18 | 3700 | 117.6 | 1.00 | 0.21 | −0.35 | 0.10 | 4 | $1.219^{\dagger}$ | 0.011 |
| HD 120933 | K5III | −0.00 | 3820 | 60.9 | 1.52 | 0.18 | +0.50 | 0.09 | 8 | $1.226^{\dagger}$ | 0.012 |
| HD 121130 | M3III | −0.24 | 3672 | 117.6 | 1.25 | 0.21 | −0.24 | 0.10 | 2 | 1.216 | 0.012 |
| HD 121299 | K2III | +2.85 | 4710 | 60.9 | 2.64 | 0.18 | −0.03 | 0.09 | 4 | $1.125^{\dagger}$ | 0.011 |
| HD 122563 | F8IV | +3.73 | 4566 | 75.0 | 1.12 | 0.40 | −2.63 | 0.15 | 4 | $1.053^{\dagger}$ | 0.011 |
| HD 122956 | G6IV-Vw | +5.89 | 4635 | 75.0 | 1.49 | 0.40 | −1.75 | 0.15 | 2 | 1.084 | 0.010 |
| HD 123299 | A0III | +3.63 | 9894 | 60.9 | 2.90 | 0.21 | +0.12 | 0.10 | 5 | 1.048 | 0.011 |
| HD 123657 | M4III | −0.23 | 3450 | 60.9 | 0.85 | 0.21 | +0.00 | 0.09 | 4 | $1.231^{\dagger}$ | 0.013 |
| HD 124186 | K4III | +3.59 | 4347 | 60.9 | 2.10 | 0.18 | +0.24 | 0.09 | 3 | 1.144 | 0.011 |
| HD 124850 | F7IV | +2.80 | 6116 | 60.9 | 3.87 | 0.18 | −0.11 | 0.09 | 3 | 1.051 | 0.009 |
| HD 124897 | K2IIIp | −2.91 | 4361 | 75.0 | 1.93 | 0.40 | −0.53 | 0.15 | 2 | 1.137 | 0.013 |
| HD 126327 | M7.5III | +1.74 | 2819 | 60.9 | 0.00 | 0.18 | −0.58 | 0.09 | 4 | $1.282^{\dagger}$ | 0.013 |
| HD 126681 | G3V | +7.63 | 5536 | 60.9 | 4.65 | 0.18 | −1.25 | 0.09 | 2 | 1.068 | 0.010 |
| HD 126778 | K0III | +5.84 | 4847 | 60.9 | 2.34 | 0.21 | −0.62 | 0.09 | 2 | 1.120 | 0.011 |
| HD 127243 | G3IV | +3.15 | 4978 | 75.0 | 3.20 | 0.40 | −0.59 | 0.15 | 3 | 1.091 | 0.012 |
| HD 130694 | K4III | +1.10 | 4040 | 60.9 | 1.85 | 0.18 | −0.34 | 0.09 | 3 | 1.173 | 0.011 |
| HD 130705 | K4II-III | +3.95 | 4336 | 60.9 | 2.10 | 0.18 | +0.41 | 0.09 | 4 | $1.151^{\dagger}$ | 0.011 |
| HD 131430 | K2/K3III | +2.20 | 4190 | 60.9 | 2.18 | 0.18 | +0.04 | 0.09 | 4 | $1.159^{\dagger}$ | 0.011 |
| HD 131918 | K4III | +2.09 | 3970 | 60.9 | 1.49 | 0.18 | +0.22 | 0.09 | 3 | 1.173 | 0.012 |
| HD 132345 | K3III-IVp | +3.26 | 4374 | 60.9 | 1.60 | 0.18 | +0.23 | 0.09 | 3 | 1.155 | 0.013 |
| HD 134063 | G5III | +5.47 | 4885 | 60.9 | 2.34 | 0.21 | −0.69 | 0.09 | 4 | $1.109^{\dagger}$ | 0.011 |
| HD 135722 | G8III | +1.22 | 4847 | 75.0 | 2.56 | 0.40 | −0.44 | 0.15 | 2 | 1.086 | 0.011 |
| HD 136726 | K4III | +1.93 | 4120 | 60.9 | 2.03 | 0.18 | +0.07 | 0.09 | 4 | $1.190^{\dagger}$ | 0.014 |
| HD 137471 | M1III | +1.03 | 3422 | 60.9 | 1.10 | 0.18 | +0.07 | 0.10 | 3 | 1.194 | 0.010 |
| HD 137704 | K4III | +2.11 | 4095 | 60.9 | 1.97 | 0.18 | −0.27 | 0.09 | 4 | $1.166^{\dagger}$ | 0.011 |
| HD 137759 | K2III | +0.77 | 4498 | 60.9 | 2.38 | 0.18 | +0.05 | 0.09 | 3 | 1.125 | 0.012 |
| HD 137909 | F0p | +3.45 | 8541 | 117.6 | 4.25 | 0.21 | +0.83 | 0.10 | 3 | 1.047 | 0.009 |
| HD 138481 | K5III | +1.21 | 3890 | 60.9 | 1.64 | 0.18 | +0.20 | 0.09 | 4 | $1.166^{\dagger}$ | 0.018 |
| HD 139641 | G7.5IIIb | +3.10 | 5030 | 60.9 | 3.22 | 0.18 | −0.55 | 0.09 | 2 | 1.081 | 0.011 |
| HD 140160 | A0p...V | +5.20 | 9164 | 117.6 | 3.30 | 0.21 | −0.25 | 0.10 | 2 | 1.050 | 0.011 |
| HD 141527 | G0Iab:pe | +4.56 | 6816 | 60.9 | 0.48 | 0.18 | −0.50 | 0.09 | 4 | 1.042 | 0.014 |
| HD 141714 | G3.5III | +2.66 | 5230 | 60.9 | 3.02 | 0.18 | −0.29 | 0.09 | 5 | 1.075 | 0.012 |
| HD 145675 | K0V | +4.71 | 5264 | 75.0 | 4.66 | 0.40 | +0.34 | 0.15 | 4 | $1.080^{\dagger}$ | 0.009 |
| HD 146051 | M0.5III | −1.17 | 3793 | 117.6 | 1.40 | 0.21 | +0.32 | 0.10 | 2 | 1.189 | 0.011 |
| HD 147923 | M... | +3.46 | 3600 | 117.6 | 0.80 | 0.21 | −0.19 | 0.10 | 4 | $1.221^{\dagger}$ | 0.011 |
| HD 148783 | M6III | +0.29 | 3279 | 112.8 | 0.20 | 0.21 | −0.06 | 0.09 | 4 | $1.249^{\dagger}$ | 0.012 |
| HD 148897 | G8pII | +1.96 | 4284 | 117.6 | 1.15 | 0.21 | −0.75 | 0.09 | 2 | 1.116 | 0.011 |
| HD 149009 | K5III | +2.04 | 3910 | 60.9 | 1.60 | 0.18 | +0.30 | 0.09 | 3 | 1.209 | 0.012 |
| HD 149661 | K0V | +3.91 | 5168 | 60.9 | 4.63 | 0.18 | +0.04 | 0.09 | 4 | $1.075^{\dagger}$ | 0.009 |
| HD 150012 | F5III-IV | +5.26 | 6505 | 60.9 | 3.90 | 0.18 | +0.16 | 0.09 | 3 | 1.058 | 0.009 |
| HD 150680 | F9IV | +1.28 | 5672 | 60.9 | 3.74 | 0.18 | +0.01 | 0.09 | 2 | 1.055 | 0.009 |
| HD 151203 | M3IIIab | +0.89 | 3640 | 60.9 | 0.70 | 0.18 | −0.10 | 0.10 | 3 | 1.218 | 0.011 |
| HD 154733 | K3III | +2.48 | 4279 | 60.9 | 2.10 | 0.18 | +0.00 | 0.09 | 4 | $1.165^{\dagger}$ | 0.011 |
| HD 155763 | B6III | +3.60 | 13397 | 117.6 | 4.24 | 0.18 | −0.95 | 0.10 | 2 | 1.049 | 0.010 |
| HD 156014 | M5Ib-II | −1.99 | 3161 | 112.8 | 0.00 | 0.21 | +0.00 | 0.09 | 2 | 1.267 | 0.012 |
| HD 156026 | K5V | +3.86 | 4541 | 60.9 | 4.54 | 0.18 | −0.37 | 0.09 | 2 | 1.106 | 0.009 |
| HD 156283 | K3IIvar | −0.02 | 4460 | 60.9 | 2.33 | 0.18 | +0.18 | 0.09 | 3 | 1.176 | 0.011 |
| HD 157910 | G5III | +4.39 | 5137 | 60.9 | 1.83 | 0.18 | −0.32 | 0.09 | 3 | 1.077 | 0.011 |
| HD 160933 | F9V | +4.82 | 5684 | 75.0 | 3.90 | 0.40 | −0.32 | 0.15 | 2 | 1.061 | 0.009 |
| HD 161096 | K2III | +0.43 | 4543 | 60.9 | 2.16 | 0.18 | +0.08 | 0.09 | 2 | 1.138 | 0.016 |
| HD 161797 | G5IV | +1.51 | 5411 | 75.0 | 3.87 | 0.40 | +0.16 | 0.15 | 3 | 1.067 | 0.010 |
| HD 161817 | A2VI(HB) | +6.29 | 7759 | 60.9 | 2.95 | 0.18 | −0.95 | 0.09 | 2 | 1.046 | 0.010 |
| HD 163990 | M6Svar | +0.19 | 3365 | 117.6 | 0.70 | 0.21 | +0.01 | 0.10 | 3 | 1.247 | 0.011 |
| HD 163993 | G8III | +1.73 | 5028 | 60.9 | 2.70 | 0.18 | +0.03 | 0.09 | 3 | 1.087 | 0.012 |
| HD 164058 | K5III | −1.16 | 3930 | 60.9 | 1.26 | 0.18 | −0.05 | 0.09 | 4 | $1.189^{\dagger}$ | 0.012 |
| HD 164136 | F2II | +2.77 | 6799 | 117.6 | 2.63 | 0.21 | −0.30 | 0.10 | 3 | 1.044 | 0.011 |
| HD 164349 | K0.5IIb | +1.93 | 4446 | 60.9 | 1.50 | 0.18 | +0.39 | 0.09 | 4 | $1.157^{\dagger}$ | 0.011 |
| HD 166208 | G8III... | +2.93 | 4919 | 75.0 | 2.52 | 0.40 | +0.08 | 0.15 | 3 | 1.075 | 0.011 |

**Table A.1.** continued.

| Name | Spectral type | $K$ (mag) | $T_{\rm eff}$ (K) | $\sigma[T_{\rm eff}]$ | $\log g$ (dex) | $\sigma[\log g]$ | [Fe/H] (dex) | $\sigma$[Fe/H] | $N$ | $D_{\rm CO}$ | $\sigma[D_{\rm CO}]$ |
|---|---|---|---|---|---|---|---|---|---|---|---|
| HD 167768 | G3III | +3.89 | 5235 | 60.9 | 1.61 | 0.21 | −0.68 | 0.09 | 4 | 1.085$^{\dagger}$ | 0.011 |
| HD 168322 | G8.5IIIb | +3.93 | 4793 | 60.9 | 2.00 | 0.18 | −0.40 | 0.09 | 3 | 1.111 | 0.012 |
| HD 168720 | M1III | +0.74 | 3810 | 60.9 | 1.10 | 0.18 | +0.00 | 0.10 | 4 | 1.211$^{\dagger}$ | 0.012 |
| HD 168723 | K0III-IV | +1.05 | 4859 | 75.0 | 3.13 | 0.40 | −0.19 | 0.15 | 2 | 1.099 | 0.011 |
| HD 173819 | K0Ibpvar | +2.15 | 4421 | 117.6 | 0.00 | 0.21 | −0.88 | 0.10 | 3 | 1.121 | 0.012 |
| HD 174638 | B7Ve.... | +3.19 | 12136 | 60.9 | 2.50 | 0.18 | +0.43 | 0.09 | 3 | 1.041 | 0.011 |
| HD 175865 | M5III | −1.83 | 3520 | 60.9 | 0.50 | 0.18 | +0.14 | 0.10 | 4 | 1.250$^{\dagger}$ | 0.012 |
| HD 181096 | F6IV: | +6.47 | 6276 | 75.0 | 4.09 | 0.40 | −0.26 | 0.15 | 2 | 1.047 | 0.009 |
| HD 182835 | F2Ib | +4.01 | 7350 | 721.4 | 2.15 | 0.32 | +0.09 | 0.29 | 2 | 1.050 | 0.010 |
| HD 184499 | G0V | +5.07 | 5738 | 100.0 | 4.02 | 0.50 | −0.66 | 0.30 | 4 | 1.044$^{\dagger}$ | 0.009 |
| HD 184786 | M4.5III | +0.74 | 3467 | 117.6 | 0.60 | 0.21 | −0.04 | 0.10 | 4 | 1.234$^{\dagger}$ | 0.012 |
| HD 185144 | K0V | +2.90 | 5260 | 75.0 | 4.55 | 0.40 | −0.24 | 0.15 | 4 | 1.061$^{\dagger}$ | 0.009 |
| HD 187216 | R... | +6.02 | 3500 | 117.6 | 0.40 | 0.21 | −2.48 | 0.10 | 4 | 1.138$^{\dagger}$ | 0.010 |
| HD 187921 | K0var | +3.80 | 6000 | 117.6 | 1.00 | 0.21 | +0.28 | 0.10 | 3 | 1.046 | 0.012 |
| HD 188119 | G8III | +1.73 | 4915 | 75.0 | 2.61 | 0.40 | −0.32 | 0.15 | 3 | 1.098 | 0.012 |
| HD 191277 | K3III | +2.72 | 4459 | 60.9 | 2.71 | 0.18 | +0.30 | 0.09 | 4 | 1.131$^{\dagger}$ | 0.011 |
| HD 195593 | F5Iab | +3.65 | 6700 | 721.4 | 1.95 | 0.18 | +0.12 | 0.09 | 3 | 1.046 | 0.012 |
| HD 199799 | M1I | +1.33 | 3400 | 117.6 | 0.30 | 0.21 | −0.24 | 0.10 | 4 | 1.241$^{\dagger}$ | 0.012 |
| HD 202447 | G0III+... | +2.34 | 6087 | 60.9 | 3.24 | 0.18 | +0.09 | 0.09 | 5 | 1.085 | 0.010 |
| HD 209369 | F5V | +3.96 | 6217 | 60.9 | 3.85 | 0.18 | −0.26 | 0.09 | 2 | 1.051 | 0.009 |
| HD 216228 | K0III | +1.27 | 4768 | 75.0 | 2.49 | 0.40 | +0.01 | 0.15 | 2 | 1.118 | 0.011 |
| HD 217382 | K4III | +1.49 | 4035 | 60.9 | 1.24 | 0.18 | −0.25 | 0.09 | 2 | 1.182 | 0.011 |
| HD 223047$^{\star}$ | G5Ib | +2.47 | 4990 | 117.6 | 1.50 | 0.21 | +0.18 | 0.10 | 2 | 1.140 | 0.010 |
| HD 232078 | K4-5III | +4.19 | 4008 | 60.9 | 0.30 | 0.18 | −1.73 | 0.09 | 4 | 1.139$^{\dagger}$ | 0.011 |

Note: Stars marked with a † symbol were observed at the TNG. AGB stars are marked with a ⋆ symbol.

**Table A.2.** Cluster stars used in the fitting function procedure.

| Name | $T_{\rm eff}$ (K) | $\sigma[T_{\rm eff}]$ | $\log g$ (dex) | $\sigma[\log g]$ | [Fe/H] (dex) | $\sigma$[Fe/H] | $D_{\rm CO}$ | $\sigma[D_{\rm CO}]$ |
|---|---|---|---|---|---|---|---|---|
| Liller1-6 | 3612 | 127.0 | +0.05 | 0.11 | −0.61 | 0.09 | 1.250 | 0.047 |
| Liller1-7 | 3671 | 96.0 | +0.07 | 0.13 | −0.61 | 0.09 | 1.178 | 0.043 |
| Liller1-157$^\star$ | 4011 | 121.0 | −0.11 | 0.11 | −0.61 | 0.09 | 1.248 | 0.047 |
| Liller1-158 | 3671 | 96.0 | −0.02 | 0.11 | −0.61 | 0.09 | 1.245 | 0.047 |
| Liller1-162 | 3627 | 119.0 | +0.29 | 0.11 | −0.61 | 0.09 | 1.214 | 0.045 |
| Liller1-166 | 3973 | 118.0 | +0.56 | 0.13 | −0.61 | 0.09 | 1.150 | 0.041 |
| Liller1-299 | 3150 | 134.0 | −0.07 | 0.11 | −0.61 | 0.09 | 1.255 | 0.047 |
| M 69-1 | 3830 | 106.0 | +0.04 | 0.10 | −0.78 | 0.03 | 1.215 | 0.023 |
| M 69-II-37 | 3716 | 97.0 | +0.09 | 0.12 | −0.78 | 0.03 | 1.178 | 0.022 |
| M 69-I-40 | 3917 | 113.0 | +0.25 | 0.12 | −0.78 | 0.03 | 1.166 | 0.022 |
| M 69-2 | 3864 | 109.0 | +0.30 | 0.11 | −0.78 | 0.03 | 1.215 | 0.023 |
| M 69-3 | 3864 | 109.0 | +0.30 | 0.11 | −0.78 | 0.03 | 1.212 | 0.023 |
| M 69-4 | 3899 | 112.0 | +0.41 | 0.12 | −0.78 | 0.03 | 1.219 | 0.024 |
| M 71-29 | 3641 | 108.0 | +0.09 | 0.12 | −0.84 | 0.06 | 1.203 | 0.017 |
| M 71-30 | 3992 | 120.0 | +0.68 | 0.13 | −0.84 | 0.06 | 1.185 | 0.016 |
| M 71-B | 3764 | 100.0 | +0.25 | 0.12 | −0.84 | 0.06 | 1.188 | 0.016 |
| M 71-46 | 4011 | 121.0 | +0.80 | 0.11 | −0.84 | 0.06 | 1.195 | 0.016 |
| M 71-A4 | 4153 | 134.0 | +0.79 | 0.13 | −0.84 | 0.06 | 1.178 | 0.016 |
| M 71-1=H | 3796 | 103.0 | +0.86 | 0.12 | −0.84 | 0.06 | 1.175 | 0.016 |
| M 71-2=I | 4565 | 173.0 | +1.08 | 0.11 | −0.84 | 0.06 | 1.149 | 0.015 |
| M 71-3=113 | 3954 | 116.0 | +0.83 | 0.13 | −0.84 | 0.06 | 1.192 | 0.016 |
| M 71-4=45 | 4011 | 121.0 | +0.87 | 0.13 | −0.84 | 0.06 | 1.171 | 0.016 |
| M 71-5=64 | 4153 | 134.0 | +1.42 | 0.10 | −0.84 | 0.06 | 1.159 | 0.016 |
| M 71-6=66 | 4649 | 182.0 | +1.39 | 0.10 | −0.84 | 0.06 | 1.137 | 0.015 |
| M 71-8=21 | 4458 | 162.0 | +1.45 | 0.13 | −0.84 | 0.06 | 1.138 | 0.015 |
| NGC 0104-A02 | 3533 | 128.0 | +0.08 | 0.13 | −0.78 | 0.02 | 1.214 | 0.035 |
| NGC 0104-W12 | 3780 | 102.0 | +0.05 | 0.10 | −0.78 | 0.02 | 1.225 | 0.036 |
| NGC 0104-A19 | 3554 | 128.0 | +0.10 | 0.12 | −0.78 | 0.02 | 1.181 | 0.034 |
| NGC 0104-V07 | 3764 | 100.0 | +0.21 | 0.13 | −0.78 | 0.02 | 1.188 | 0.034 |
| NGC 0104-V06 | 3864 | 109.0 | +0.43 | 0.12 | −0.78 | 0.02 | 1.172 | 0.033 |
| NGC 0104-L168 | 3882 | 110.0 | +0.43 | 0.12 | −0.78 | 0.02 | 1.215 | 0.035 |
| NGC 0104-5529 | 3973 | 118.0 | +0.64 | 0.13 | −0.78 | 0.02 | 1.205 | 0.035 |
| NGC 0104-2426 | 4070 | 126.0 | +0.93 | 0.12 | −0.78 | 0.02 | 1.170 | 0.033 |
| NGC 0104-1505 | 4070 | 126.0 | +0.96 | 0.12 | −0.78 | 0.02 | 1.184 | 0.034 |
| NGC 0104-4418 | 4091 | 128.0 | +0.95 | 0.11 | −0.78 | 0.02 | 1.188 | 0.034 |
| NGC 0104-1510 | 4153 | 134.0 | +1.01 | 0.14 | −0.78 | 0.02 | 1.168 | 0.033 |
| NGC 0104-2416 | 4219 | 140.0 | +1.33 | 0.15 | −0.78 | 0.02 | 1.177 | 0.034 |
| NGC 0104-6408 | 4383 | 155.0 | +1.44 | 0.14 | −0.78 | 0.02 | 1.163 | 0.033 |
| NGC 0288-A96 | 4070 | 126.0 | +0.50 | 0.10 | −1.14 | 0.03 | 1.144 | 0.016 |
| NGC 0288-A78 | 4132 | 132.0 | +0.67 | 0.11 | −1.14 | 0.03 | 1.148 | 0.016 |
| NGC 0288-C20 | 4153 | 134.0 | +0.71 | 0.11 | −1.14 | 0.03 | 1.118 | 0.015 |
| NGC 0288-A77 | 4219 | 140.0 | +0.83 | 0.10 | −1.14 | 0.03 | 1.135 | 0.016 |
| NGC 0288-A245 | 4433 | 160.0 | +1.10 | 0.12 | −1.14 | 0.03 | 1.124 | 0.015 |
| NGC 0362-III11 | 4011 | 121.0 | +0.37 | 0.10 | −1.09 | 0.03 | 1.162 | 0.035 |
| NGC 0362-IV100 | 4091 | 128.0 | +0.50 | 0.10 | −1.09 | 0.03 | 1.145 | 0.034 |
| NGC 0362-III63 | 4031 | 123.0 | +0.52 | 0.10 | −1.09 | 0.03 | 1.169 | 0.036 |
| NGC 0362-III44 | 4091 | 128.0 | +0.66 | 0.10 | −1.09 | 0.03 | 1.119 | 0.033 |
| NGC 0362-III70 | 4310 | 148.0 | +0.75 | 0.10 | −1.09 | 0.03 | 1.088 | 0.031 |
| NGC 5927-100$^\star$ | 3847 | 107.0 | +0.01 | 0.11 | −0.64 | 0.01 | 1.246 | 0.046 |
| NGC 5927-799 | 3847 | 107.0 | +0.38 | 0.12 | −0.64 | 0.01 | 1.243 | 0.045 |
| NGC 5927-627 | 3864 | 109.0 | +0.51 | 0.11 | −0.64 | 0.01 | 1.203 | 0.043 |
| NGC 5927-532 | 3992 | 120.0 | +0.80 | 0.12 | −0.64 | 0.01 | 1.167 | 0.041 |
| NGC 5927-622 | 4175 | 136.0 | +1.00 | 0.15 | −0.64 | 0.01 | 1.152 | 0.040 |
| NGC 5927-536 | 4310 | 148.0 | +1.27 | 0.15 | −0.64 | 0.01 | 1.191 | 0.042 |
| NGC 6388-1 | 3954 | 116.0 | −0.34 | 0.13 | −0.74 | 0.18 | 1.238 | 0.038 |
| NGC 6388-3 | 3899 | 112.0 | −0.05 | 0.11 | −0.74 | 0.18 | 1.230 | 0.038 |
| NGC 6388-4 | 3701 | 96.0 | +0.09 | 0.13 | −0.74 | 0.18 | 1.204 | 0.037 |
| NGC 6440-KF-1 | 3847 | 107.0 | +0.41 | 0.13 | −0.62 | 0.10 | 1.179 | 0.018 |
| NGC 6440-KF-2 | 3813 | 105.0 | +0.46 | 0.11 | −0.62 | 0.10 | 1.210 | 0.018 |
| NGC 6440-KF-3 | 3716 | 97.0 | +0.47 | 0.12 | −0.62 | 0.10 | 1.196 | 0.018 |
| NGC 6440-KF-4 | 3686 | 94.0 | +0.50 | 0.12 | −0.62 | 0.10 | 1.193 | 0.018 |
| NGC 6440-KF-5 | 3864 | 109.0 | +0.53 | 0.11 | −0.62 | 0.10 | 1.239 | 0.019 |
| NGC 6440-KF-6 | 3747 | 99.0 | +0.57 | 0.12 | −0.62 | 0.10 | 1.188 | 0.018 |
| NGC 6440-KF-8 | 3747 | 99.0 | +0.67 | 0.11 | −0.62 | 0.10 | 1.196 | 0.018 |
| NGC 6440-KF-7 | 3796 | 103.0 | +0.67 | 0.12 | −0.62 | 0.10 | 1.201 | 0.018 |
| NGC 6528-7 | 3864 | 109.0 | +0.30 | 0.11 | −0.61 | 0.08 | 1.220 | 0.029 |

**Table A.2.** continued.

| Name | $T_{\text{eff}}$ (K) | $\sigma[T_{\text{eff}}]$ | $\log g$ (dex) | $\sigma[\log g]$ | [Fe/H] (dex) | $\sigma$[Fe/H] | $D_{\text{CO}}$ | $\sigma[D_{\text{CO}}]$ |
|---|---|---|---|---|---|---|---|---|
| NGC 6528-11 | 3732 | 98.0 | +0.05 | 0.11 | −0.61 | 0.08 | 1.242 | 0.030 |
| NGC 6528-22⋆ | 3813 | 105.0 | +0.37 | 0.12 | −0.61 | 0.08 | 1.275 | 0.031 |
| NGC 6528-6⋆ | 3917 | 113.0 | +0.41 | 0.12 | −0.61 | 0.08 | 1.248 | 0.030 |
| NGC 6553-20 | 3780 | 102.0 | −0.16 | 0.12 | −0.60 | 0.04 | 1.209 | 0.034 |
| NGC 6553-19 | 3551 | 138.0 | −0.02 | 0.10 | −0.60 | 0.04 | 1.227 | 0.035 |
| NGC 6553-25 | 3747 | 99.0 | +0.14 | 0.14 | −0.60 | 0.04 | 1.229 | 0.036 |
| NGC 6553-16⋆ | 3917 | 113.0 | +0.27 | 0.11 | −0.60 | 0.04 | 1.288 | 0.038 |
| NGC 6553-26⋆ | 3847 | 107.0 | +0.32 | 0.13 | −0.60 | 0.04 | 1.281 | 0.038 |
| NGC 6553-14⋆ | 3813 | 105.0 | +0.38 | 0.12 | −0.60 | 0.04 | 1.265 | 0.037 |
| NGC 6553-2 | 3656 | 105.0 | +0.42 | 0.12 | −0.60 | 0.04 | 1.192 | 0.034 |
| NGC 6624-KF-1 | 3917 | 113.0 | +0.40 | 0.11 | −0.70 | 0.03 | 1.230 | 0.034 |
| NGC 6624-KF-2 | 3917 | 113.0 | +0.53 | 0.13 | −0.70 | 0.03 | 1.160 | 0.030 |
| NGC 6624-KF-3 | 3917 | 113.0 | +0.54 | 0.13 | −0.70 | 0.03 | 1.162 | 0.030 |
| NGC 6624-KF-4 | 3899 | 112.0 | +0.82 | 0.14 | −0.70 | 0.03 | 1.218 | 0.033 |
| NGC 6624-KF-5 | 4070 | 126.0 | +0.96 | 0.15 | −0.70 | 0.03 | 1.197 | 0.032 |
| NGC 6712-LM5⋆ | 4111 | 130.0 | +0.55 | 0.10 | −0.94 | 0.03 | 1.223 | 0.024 |
| NGC 6712-LCO1 | 4132 | 132.0 | +0.58 | 0.11 | −0.94 | 0.03 | 1.211 | 0.023 |
| NGC 6712-LCO3 | 4219 | 140.0 | +0.61 | 0.10 | −0.94 | 0.03 | 1.188 | 0.023 |
| NGC 6712-LM8 | 4111 | 130.0 | +0.71 | 0.11 | −0.94 | 0.03 | 1.157 | 0.022 |
| NGC 6712-LM10 | 4264 | 144.0 | +0.72 | 0.10 | −0.94 | 0.03 | 1.194 | 0.023 |
| NGC 6712-B66 | 4196 | 138.0 | +0.85 | 0.12 | −0.94 | 0.03 | 1.195 | 0.023 |
| Terzan2-1 | 4241 | 142.0 | +0.40 | 0.10 | −0.65 | 0.14 | 1.158 | 0.034 |
| Terzan2-2 | 3973 | 118.0 | +0.41 | 0.11 | −0.65 | 0.14 | 1.205 | 0.037 |
| Terzan2-3⋆ | 3899 | 112.0 | +0.43 | 0.12 | −0.65 | 0.14 | 1.260 | 0.040 |
| Terzan2-4 | 4175 | 136.0 | +0.44 | 0.11 | −0.65 | 0.14 | 1.215 | 0.037 |
| Terzan2-5 | 3936 | 115.0 | +0.56 | 0.12 | −0.65 | 0.14 | 1.200 | 0.037 |
| Terzan2-7 | 4111 | 130.0 | +0.61 | 0.10 | −0.65 | 0.14 | 1.199 | 0.037 |
| Terzan2-8 | 4132 | 132.0 | +0.62 | 0.10 | −0.65 | 0.14 | 1.151 | 0.034 |

Note: AGB stars are maked with a ⋆ symbol.